SIMULATION OF CYLINDER FLOWS WITH GAPS

by

Matthew Liu

A Thesis

Submitted to the Faculty of Purdue University

In Partial Fulfillment of the Requirements for the degree of

Master of Science

School of Aeronautics and Astronautics

West Lafayette, Indiana

May 2021

THE PURDUE UNIVERSITY GRADUATE SCHOOL
STATEMENT OF COMMITTEE APPROVAL

Dr. Jonathan Poggie, Chair

School of Aeronautics and Astronautics

Dr. Gregory Blaisdell

School of Aeronautics and Astronautics

Dr. Joseph Jewell

School of Aeronautics and Astronautics

Approved by:

Dr. Gregory Blaisdell

ACKNOWLEDGMENTS

This research was funded by the Air Force Research Laboratory under the Development of Hypersonic Vehicle Flight Test Structure project, Grant Number FA8650-19-C-2404. This thesis was cleared on 06 May 2021, Originator Reference Number RQ-21-183, Case Number AFRL-2021-1353. The author would like to thank Professors Jonathan Poggie and Gregory Blaisdell for their weekly guidance and Professor Joseph Jewell for being part of the thesis committee. Thanks also to the other students in the research group for their insights and suggestions, as well as Autumn Garner from UTSI for providing the experimental data. Finally, the author thanks his father for his continued support in this field.

TABLE OF CONTENTS

LIST OF TABLES

LIST OF FIGURES

ABSTRACT

This thesis presents results of computations of supersonic flow over finite cylinders with varying geometries at the cylinder-wall juncture. The flow domain and geometries were modeled after experiments conducted at University of Tennessee Space Institute (UTSI). CREATE Kestrel (KCFD) was used to perform improved-delayed detached eddy simulations (ID DES) of the unsteady flow. Time-accurate data were collected via taps along the centerline, partially on the surface of the cylinder geometries and on the wall upstream of the cylinder. Spectra of the pressure signals and two-point correlations were computed to compare the flow between the different cases consisting of a baseline cylinder, the cylinder with a smaller gap, and the cylinder with a wider fairing. Properties on the cylinder surface for the gap case had the greatest difference compared to the others. In addition, the spectral content showed higher frequency activity for the gap case on the surface in front of the cylinder.

1. INTRODUCTION

Supersonic flow in front of a blunt fin on a body can be highly unsteady and poses many design challenges, such as those associated with the fluctuating pressure load on the surface or localized high heat transfer rates. Over the past several decades, many experimental and computational studies have been performed to analyze the flow structures and shock wave-boundary layer interactions associated with this configuration. The wall pressure field was shown to be intermittent in front of a forward facing step by Kistler, a result of the large-scale unsteadiness of the separation at the shock foot [7]. The flow along the centerline in front of a blunt fin has shown similar characteristic traits as the step, including the intermittent pressure fluctuations beneath the shock foot [13]. Additional studies using a semi-infinite hemi-cylindrical leading edge and adiabatic wall have been performed to correlate geometric dimensions such as the leading-edge diameter and boundary layer height with the flow characteristics. Dolling and Bogdonoff collected wall pressure distributions with varying leading-edge diameter fins and boundary layer thicknesses [4]. They concluded that the leading-edge diameter was the primary variable that controlled flow field features measured by x/D (distance from the cylinder divided by the diameter) for general semi-infinite cylinders on the centerline, while the boundary layer thickness had second-order effects on the interaction scale and characteristics. Although the effect of the boundary layer should not be ignored, the primary variable in consideration is still the leading edge diameter. Therefore, near the centerline of the flow, where the greatest intensity of fluctuating pressure is expected, using a cylinder is a good approximation for a blunt fin.

Analyzing the pressure fluctuations by calculating the power spectral densities and two-point correlations in the unsteady flow is one way to quantify and compare flow regimes under different conditions. Separation unsteadiness has been found to have generally similar characteristics in a wide range of conditions in compressible flow [11]. While the probability density function of the pressure signal is approximately Gaussian in most areas of the flow, the intermittent region beneath the shock foot has been shown to be bimodal as the shock oscillates about a stationary location [2]. The intermittency can be described by the flow taking on the attributes ahead of and behind the shock depending on where the shock foot

is at a given point in time. One observation noted by Settles was the gradual separation behind the shock [12]. This region can be characterized by its own flow behavior which differs considerably compared to the areas directly upstream of the shock and downstream around reattachment under a vortex. This vortex resulting from the reattachment accompanied by reversed flow on the surface is characterized by a horseshoe shape that starts in front of the root and travels outward and downstream [9]. Each characteristic region on the surface exhibits corresponding characteristic behavior in the pressure fluctuations that can be captured with spectral analysis and two-point correlations.

Discrepancies do arise between experimental and computational data when comparing this type of flow in front of a blunt fin. Most equilibrium-based turbulence models struggle to account for the large-scale unsteadiness and three-dimensionality of the flow field [13]. Predicting the location of the shock foot and quantifying the pressure fluctuations is useful for design applications in mitigating the associated fatigue loading, and accurately doing so should still be pursued. Brusniak and Dolling collected two-point correlations of the pressure fluctuations in front of a hemi-cylindrical leading edge fin to observe the relationship between various areas in the flow [1]. They showed that fluctuations in the undisturbed turbulent boundary layer are correlated with fluctuations in the pressure behind the shock in the separated region. Their cross-correlations showed the existence of a broad mode associated with low-frequency content of the signals and a sharp mode associated with the high frequencies.

The University of Tennessee Space Institute (UTSI) conducted experimental studies on flow over a finite cylinder with various gap geometries [6], some of which were recreated here computationally. A configuration of the wind tunnel can be seen in Fig. 1.1. Introducing changes to the geometry such as a gap or fairing under the base of a cylinder changes the flow properties including the mean shock foot location, wall heat transfer rates, and skin friction coefficients in different areas. To briefly summarize the experiment performed by UTSI, washers of varying diameter were added underneath a solid cylinder to vary the size of the gap underneath the cylinder incrementally. This effectively changes the leading-edge diameter for a finite portion of the cylinder, modifying the flow properties near the cylinder-wall juncture. Using pressure-sensitive paint (PSP), the pressure fluctuations over time were

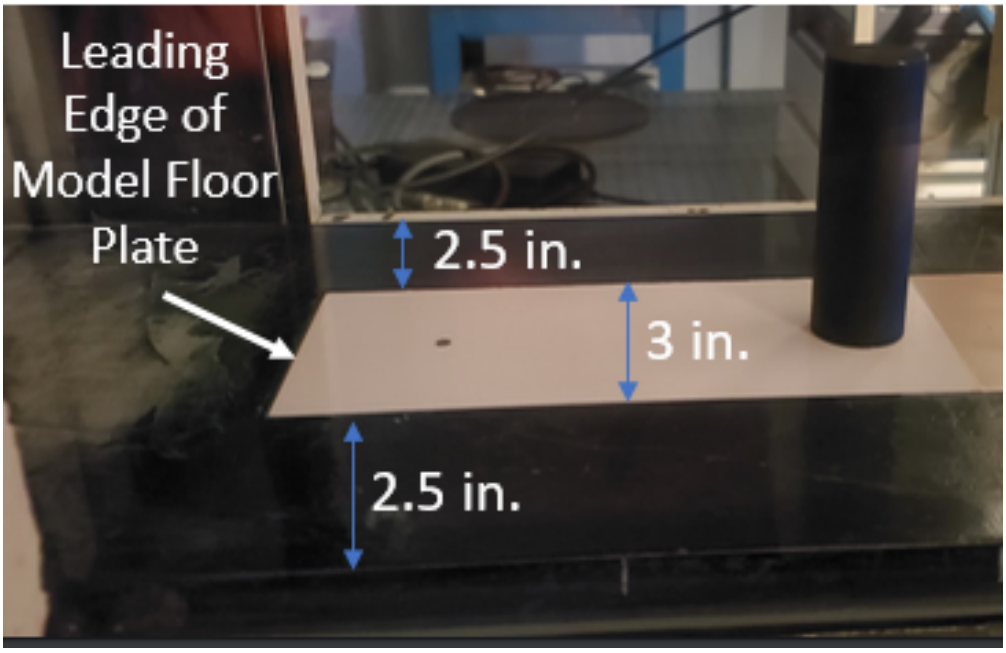

Figure 1.1 Cylinder and flatplate configuration in wind tunnel.

recorded on a removable flat plate in front of the cylinder while Schlieren photographs were taken concurrently. A light source is shone onto the PSP, which reflects at different intensities depending on the air pressure and temperature, although the temperature should ideally be kept constant. A camera captures the reflected light off the flat plate, producing a series of images corresponding to the pressure fluctuation. From this, the spectra of the pressure signals were calculated at specified locations, and schlieren photos were observed to show the differences in the flow structures.

The primary objective of this research is to identify and quantify the differences associated with modifications to the geometry at the root of of a cylinder to emulate potential design options. In this thesis, the methodology is explained by describing the meshing procedure, identifying the settings used in the solver, and listing the flow parameters used. The discussion of results starts out with an overview of the flow visualization on the surfaces and the differences between each case. Then, the power spectral densities taken at tap locations along the centerline are analyzed and compared with those from the experiment as well as between each of the three cases. Lastly, various arrangements of two-point correlations along the centerline and in the span-wise direction are calculated and explained.

2. COMPUTATIONAL SETUP

2.1 Geometries

The baseline cylinder under analysis had a diameter of 1 inch and height of 3 inches. It was fixed vertically to a flat plate on the floor of the wind tunnel, emulating a blunt fin fixed to a fuselage. There were two modifications at the cylinder-wall juncture to create three total cases for comparison. The first was the introduction of a smaller cylinder with a diameter of 0.5 inches and a height of 0.5 inches. This smaller cylinder was placed concentrically underneath the baseline cylinder, and this configuration will be referred to as the cylinder-gap case. Similarly, a larger cylinder with a diameter of 2 inches and height of 0.5 inches was configured under the baseline cylinder to create the cylinder-fairing case. A summary of the geometries is shown in Fig. 2.1. To attempt to emulate the boundary layer in the wind tunnel, the bottom wall was extended 20 inches upstream of the center of the cylinder. The width and height of the rectangular flow domain was 8 inches, with a total length of 24 inches. The actual reported boundary layer from the experiments was 11 mm, about 2 times the thickness from the computation, which was 5.57 mm at $x/d = -2.5$.

2.2 Grid Generation

Each of the three-dimensional grids were created using Pointwise®. The flow domain was divided as illustrated in Fig. 2.2. The grid begins with coarse cells in the x-direction that

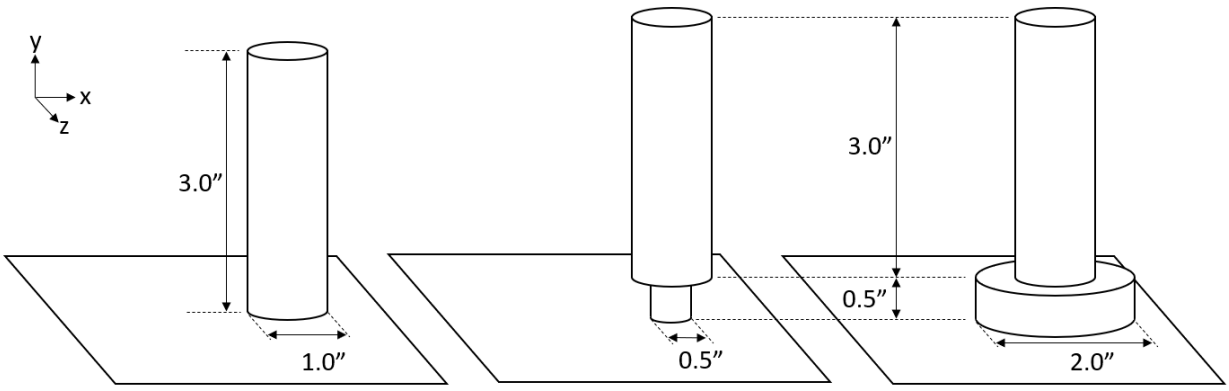

Figure 2.1 Line drawings of the three geometries.

are refined as the flow nears the cylinder. The grids are structured, and the y-direction cell spacing near the cylinder matches the cell spacing at the inlet. The first grid point off of each wall was set to 0.0003 inches, or 7.62E-6 meters, yielding a y^+ value close to 1. Wall functions were not used, even though they generally are turned on for this type of calculation for at least the first cell, so the first cell height was made an order of magnitude smaller than the suggested height of $\Delta y/\delta = 0.01$ with the intention of accommodating the lack of a wall model [10]. The actual ratio of the first cell height to the boundary layer thickness was 1.37E-3. Hyperbolic tangent scaling was used to distribute the remaining grid points in the domain off each wall surface, resulting in the boundary layer containing 50 points. From the surface of the cylinder, the grid grows radially to twice the cylinder's radius. The grid structure is extruded upward to the top of the flow domain to fill in the area above the cylinder. For the cylinder-gap case, the volume beneath the baseline cylinder was extruded inwards from the circumferential surface. The cylinder-fairing case could be described by translating the volume containing the outer-cylinder domain upwards. The cylindrical domain is placed into the rectangular domain by splitting the cylinder into fourths around the circumference, and creating a 5-way junction at each of the points. From a perspective above the flow domain, the grid appears to be split into a 3x3 configuration with the circular domain in the center, as seen in Fig. 2.2. The domain is then split in half along the xy-plane so that the grid cell dimensions about the center line can be enforced. A close-up of the gap in the cylinder-gap case can be seen in Fig. 2.3. Likewise, the cylinder-fairing configuration is shown in Fig. 2.4. Some domains were hidden in the figures for clarity so that the cells near the wall can be seen. The first cell width restriction was extended perpendicularly from each edge to keep the grid structured. In total, each domain contained about 260 million cells.

2.3 Flow parameters

The flow conditions for each of the three cases are presented in Table 2.1. While some of the properties such as the Mach number and wall temperature were fixed, the stagnation properties varied slightly when the experiment was conducted, so the values from each experimental case were used.

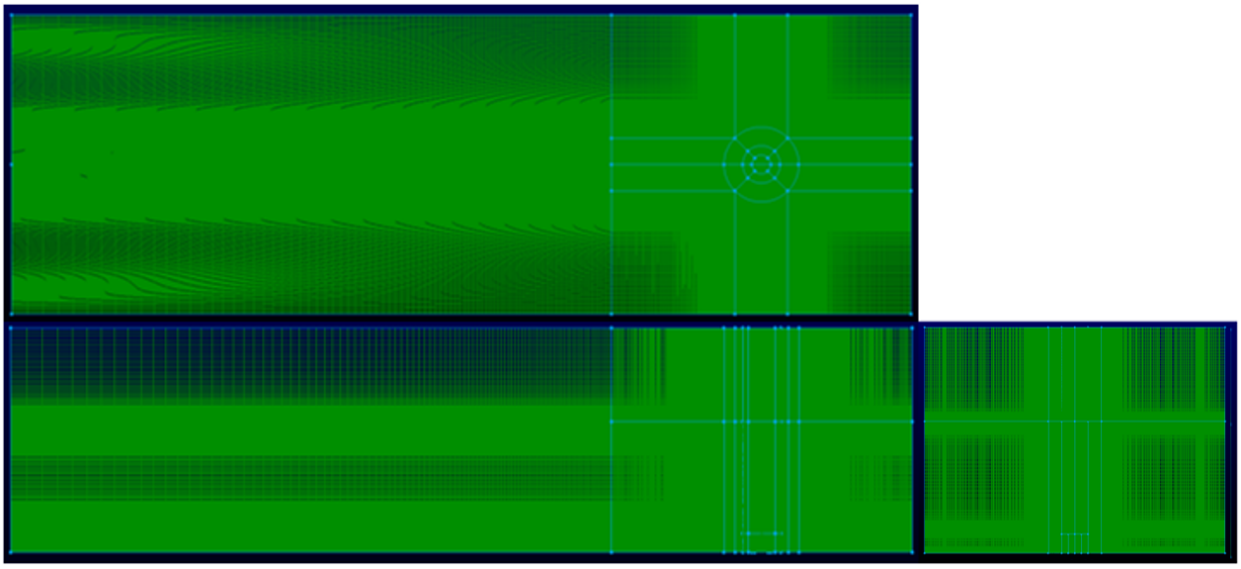

Figure 2.2 3-view of cylinder-gap grid.

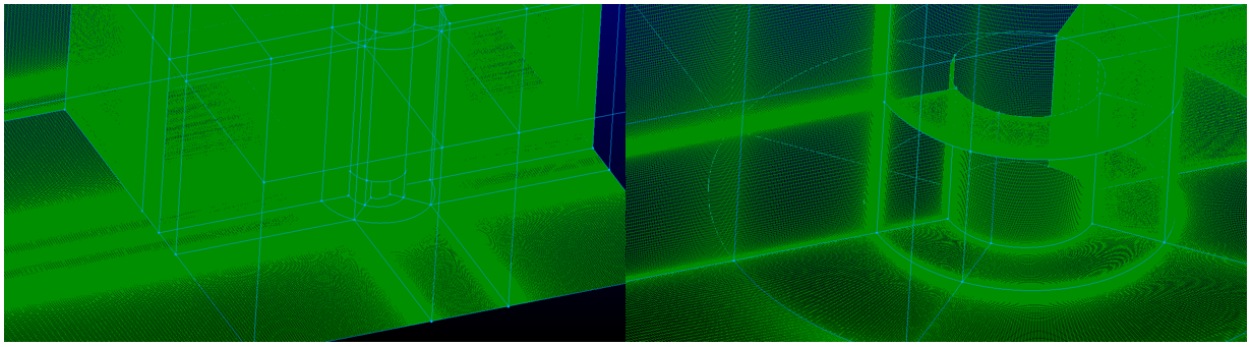

Figure 2.3 Zoomed isometric view near the gap of cylinder-gap grid.

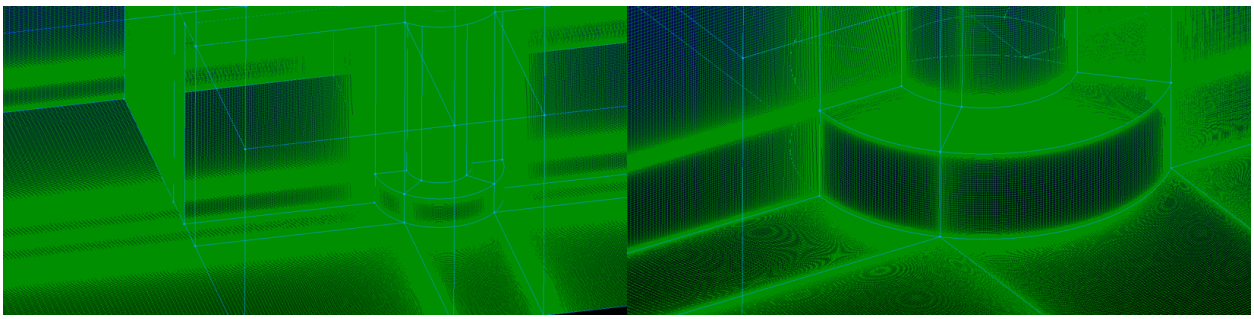

Figure 2.4 Zoomed isometric view near the gap of cylinder-fairing grid.

Table 2.1 Flow conditions for each case.

Case	P_0 [Pa]	T_0 [K]	Mach	Isothermal Wall [K]
Baseline Cylinder	243000	288	2.01	285
Cylinder with Gap	247000	290	2.01	285
Cylinder with Fairing	242000	289	2.01	285

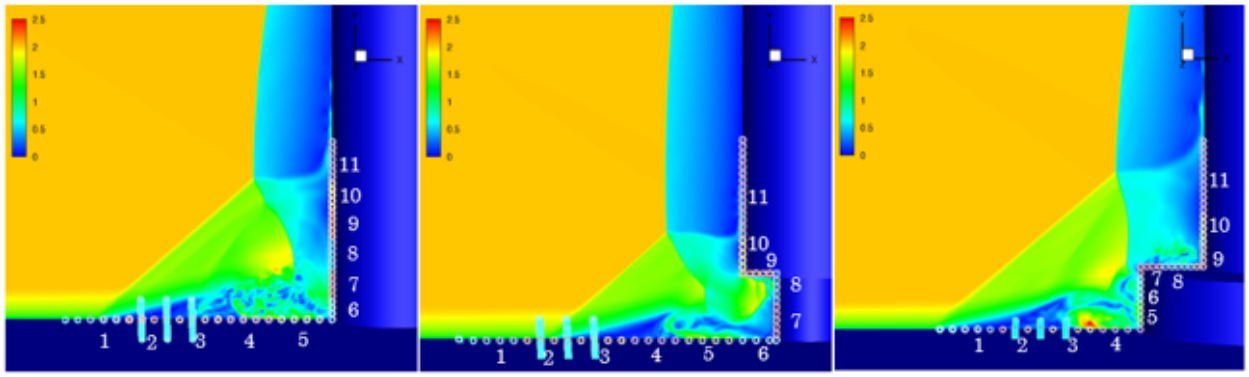

Figure 2.5 Stations of taps displayed on Mach contours.

Table 2.2 First tap in each group for baseline cylinder.

Group	x-coordinate [in]	x/D
1	17.6	-1.9
2	17.9	-1.6
3	18.3	-1.2
4	18.7	-0.8
5	19.1	-0.4
6	19.5	0

2.4 Numerical Approach

The software used for computations was CREATE Kestrel version 11.1, with KCFD the selected solver. The code is second-order accurate in time and space throughout the entire domain. Most settings were left on default, and can be assumed so if not specified otherwise. The Spalart-Allamaras (SA) turbulence model was selected for the computation, accompanied by the Menter 1-equation transition model. Quadratic Constituent Relations (QCR) were turned on to improve the accuracy of the three-dimensional flow [14]. Improved-Delay Detached Eddy Simulation (IDDES) was used to find a time-accurate solution of the unsteady flow, with each time step being 1E-6 seconds, resulting in a nondimensional time step of 0.01 (multiplying by sound speed of 242.8 and dividing by length scale of 0.0254 meters). Three sub-iterations were used for the unsteady flow, and the selected CFL number was 1. For each case, 131072 (or 2^{17}) time steps were recorded at each of the tap locations. Two boundary conditions were specified, *wall* and *farfield*. The *wall* constitutes the flat plate and cylinder configurations, all defined by the isothermal wall boundary. The *farfield* comprises the inlet, outlet, top and side surfaces, using Modified Riemann Invariants. Kestrel automatically determines if flow is entering or exiting each of the domains in the farfield. Finer grids were desired to keep the aspect ratios from the hyperbolic tangent scaling as small as possible, but this goal was somewhat hindered by a limitation of about 300 million cells in the current version of Kestrel. The transients in the simulation from startup lasted about 2000 iterations, as the residuals were steadily decreasing until that point. In order to collect a statistically stationary pressure signal, 5000 startup iterations were used that are not included in the data analysis.

2.5 Tap locations

The tap locations where pressure data were collected over 131,072 time steps are presented in Fig. 2.5, displayed on Mach contours to show their locations relative to flow structures. The location of the first, most-upstream tap is the same on each case. Likewise, the last tap on the cylinder face of each case is located 1.5 inches (38.1mm) above the wall in every case. Additional taps are introduced in the gap and fairing case by adding tap locations near the root where needed. The 3 span-wise clusters of taps that straddle the cylinder-gap shock foot location are in the same absolute location in all the cases as well. As for the 11 groupings of taps, they begin upstream with the first group comprising the third through the fifth taps. Each subsequent group from group 2 to 6 contains the next 4 taps in the sequence. Groups 7 through 10 consist of the next 5 taps in sequence, as they are clustered closer together on the cylinder face. Group 11 consists of all the remaining taps on the cylinder face, and have more tap locations on the gap and fairing cases than the baseline cylinder case. The first 2 taps act as a buffer and are needed for the two-point correlations that were calculated, as each point needed a tap located 2 spaces upstream, requiring the extra taps in front. Table 2.2 lists the tap locations of the most upstream tap in each group for the first 6 groups on the baseline cylinder case, from the free stream to the cylinder root.

3. DISCUSSION OF RESULTS

3.1 Flow Visualization

Several hundred full-visualization output files were collected. This was enough to create short movies to visualize the general behavior of the flow field without unnecessarily consuming large amounts of computational resources and disk storage. The visualization was disabled after collecting an adequate number of frames, while the data collection at the taps was continued for the remainder of the computations. The pressure was saved at each tap to collect a signal that could be used to create power spectra and two-point correlations which will be discussed later.

The overall structure of the three flow fields was compared by examining the visualization. The pressure contour at an arbitrary time are presented in Fig. 3.1 along with the streamlines

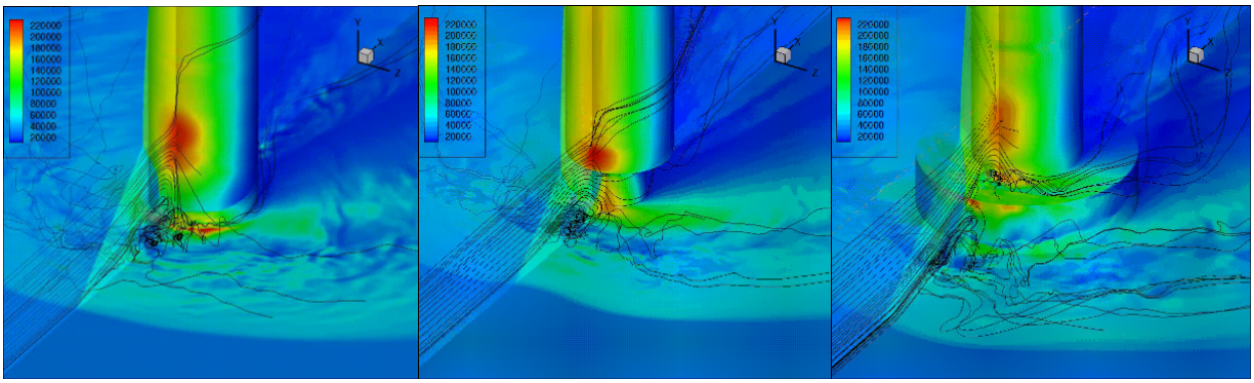

Figure 3.1 Pressure $[Pa]$ contours with streamlines.

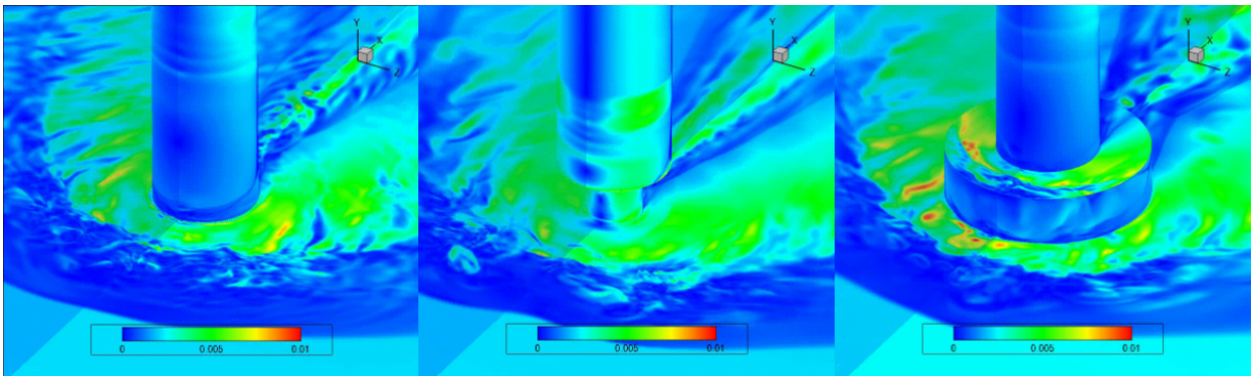

Figure 3.2 Skin friction coefficient magnitude contours of sample flow.

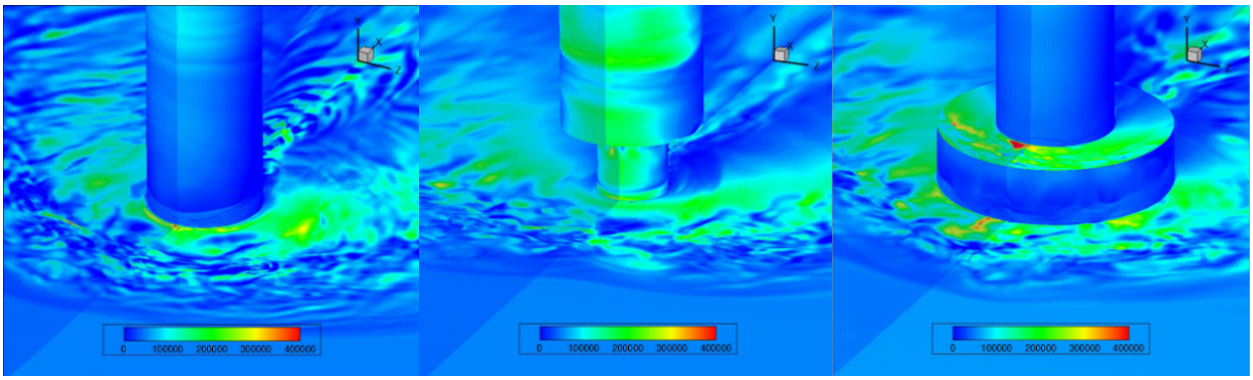

Figure 3.3 Wall heat flux $[W/m^3]$ contours of sample flow.

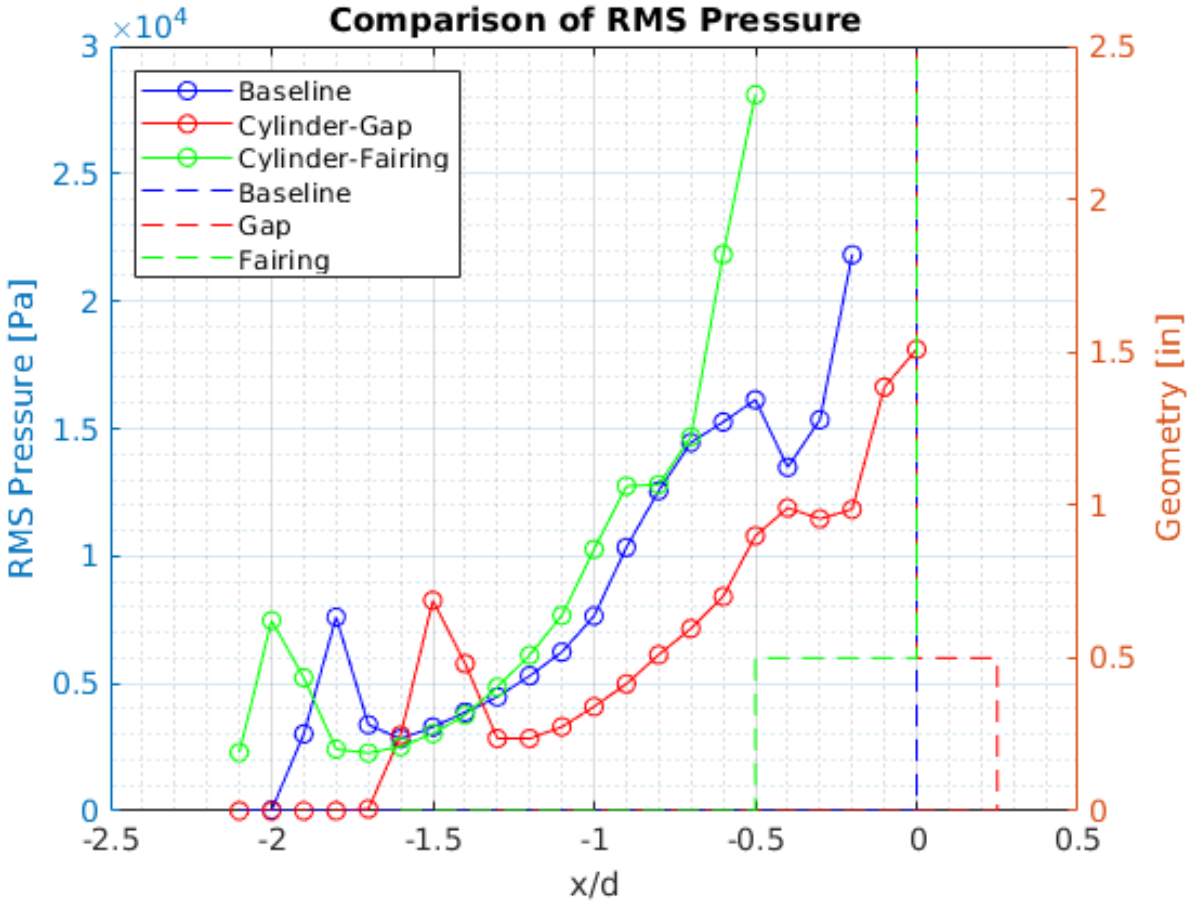

Figure 3.4 Root mean square pressure relative to geometry ($d = 1$ inch).

of the flow. The unsteady vortex structures behind the shock can be clearly seen from the streamlines. The high-pressure regions where the lambda shock impinges on the cylinder are slightly different for each case. the region of high pressure appears smaller on the cylinder-gap case compared to the baseline cylinder and slightly less intense on the cylinder-fairing case. The skin friction coefficient magnitude can be seen in Fig. 3.2, and the wall heat flux contours for a point in time are shown in Fig. 3.3. The shock separation is clearly illustrated in the skin friction contours where the entire region directly behind the shock shows a value close to 0. The reattachment and resulting horseshoe vortex structures appear on the skin friction contours as the green region corresponding to a value close to 0.005. A difference can be seen in the wake of the flows, particularly in the skin friction contours. The baseline cylinder shows distinct wave-like structures trailing behind the cylinder, with clear peaks and troughs in the values as the waves propagate downstream. Meanwhile, the cylinder-gap case shows straight streak-like structures trailing behind the cylinder, where the skin friction values seem to vary less significantly in the x-direction with time. Finally, the cylinder-fairing case exhibits larger trailing structures than the the waves from the baseline cylinder. Another observation to note is that the skin friction and wall heat flux are higher on the lower half of the cylinder in the gap case, and lower on the cylinder overall on the fairing case. However, the cylinder-fairing case appeared to show higher instantaneous heating on the horizontal surface in front of and on top of the fairing near the centerline. This difference is important in choosing where to apply thermal protection systems, as the surfaces with greater heating are not the same in each case.

The RMS values of the pressure fluctuations at the taps along the centerline are presented in Fig. 3.4. The mean separation shock foot location is indicated by the initial peak, where the pressure has the greatest local variance as it changes depending on which side of the shock it is on. The cylinder-gap case shows a more dramatic downstream shift in the mean shock foot location than the upstream shift of the cylinder-fairing case. The pressure variation is generally more intense closer to the cylinder-wall juncture. Behind the shock, the variation is less intense for the cylinder-gap case. Each case exhibits a small bump before reaching the juncture due to the reattachment of the primary separation vortex behind the shock. The

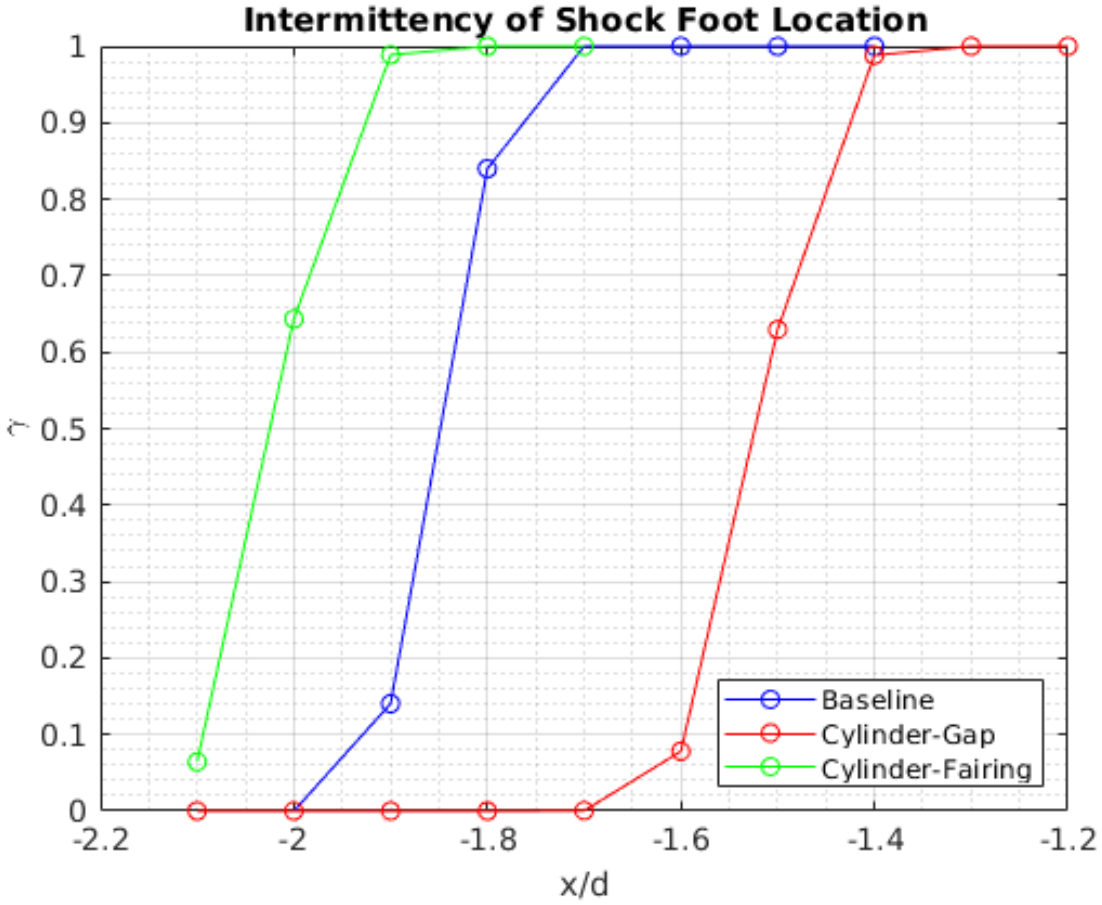

Figure 3.5 Plot of intermittency of shock foot locations for each case.

profiles of the geometry are plotted in their actual location relative to the RMS pressure values for reference.

The intermittency of the the shock foot locations can be seen in Fig. 3.5. This was found by taking the percentage of the time that a signal was above a certain pressure threshold at each tap location. Dolling and Or defined the threshold as 3 standard deviations above of the freestream pressure [2], but that value is effectively zero for the computation since a RANS model holds in the incoming boundary layer (as can be seen in the baseline and gap cases for RMS pressure; unfortunately, the upstream-most tap for the fairing case was not in the undisturbed boundary layer). Therefore, the threshold was set at 33000 Pa, about 10 percent greater than the freestream pressure.

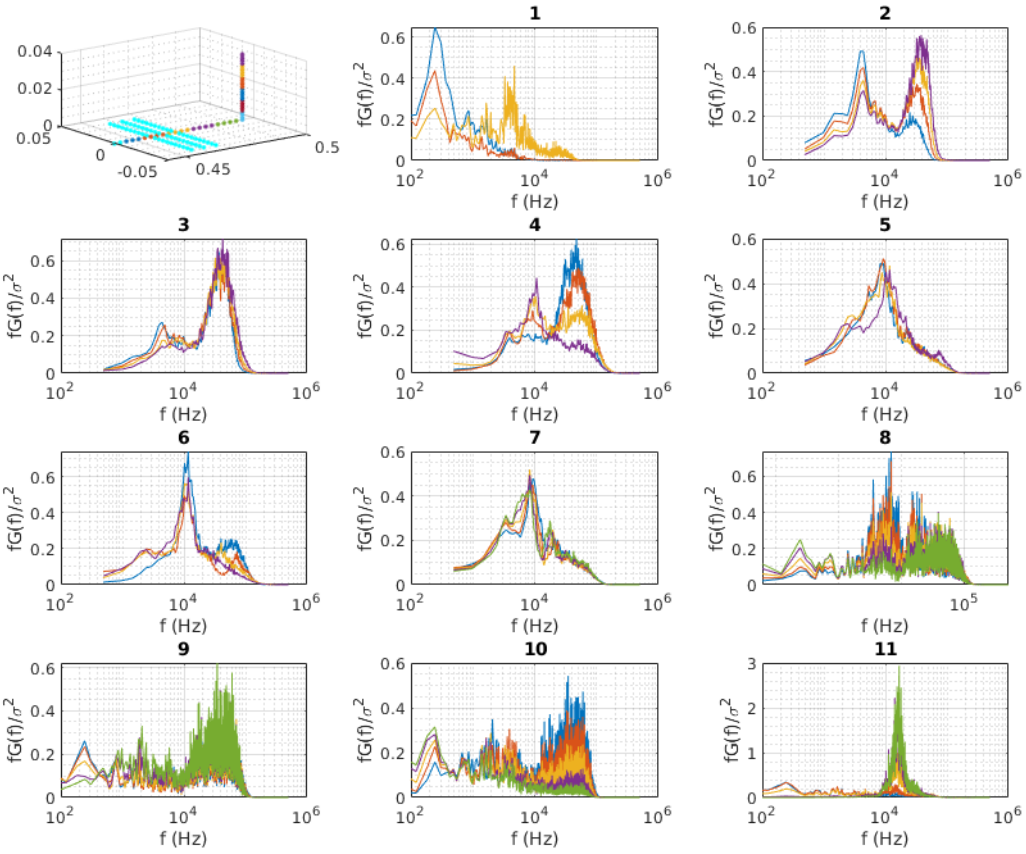

Figure 3.6 Power spectral density for baseline cylinder flow.

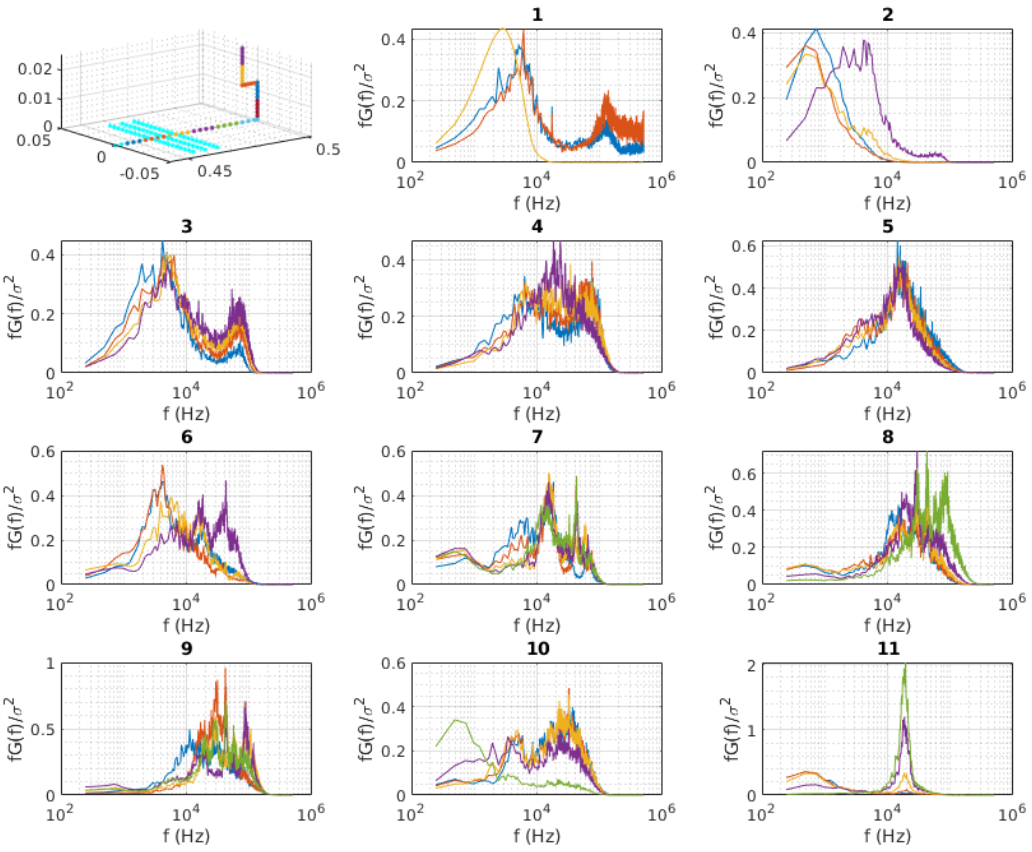

Figure 3.7 Power spectral density for cylinder-gap flow.

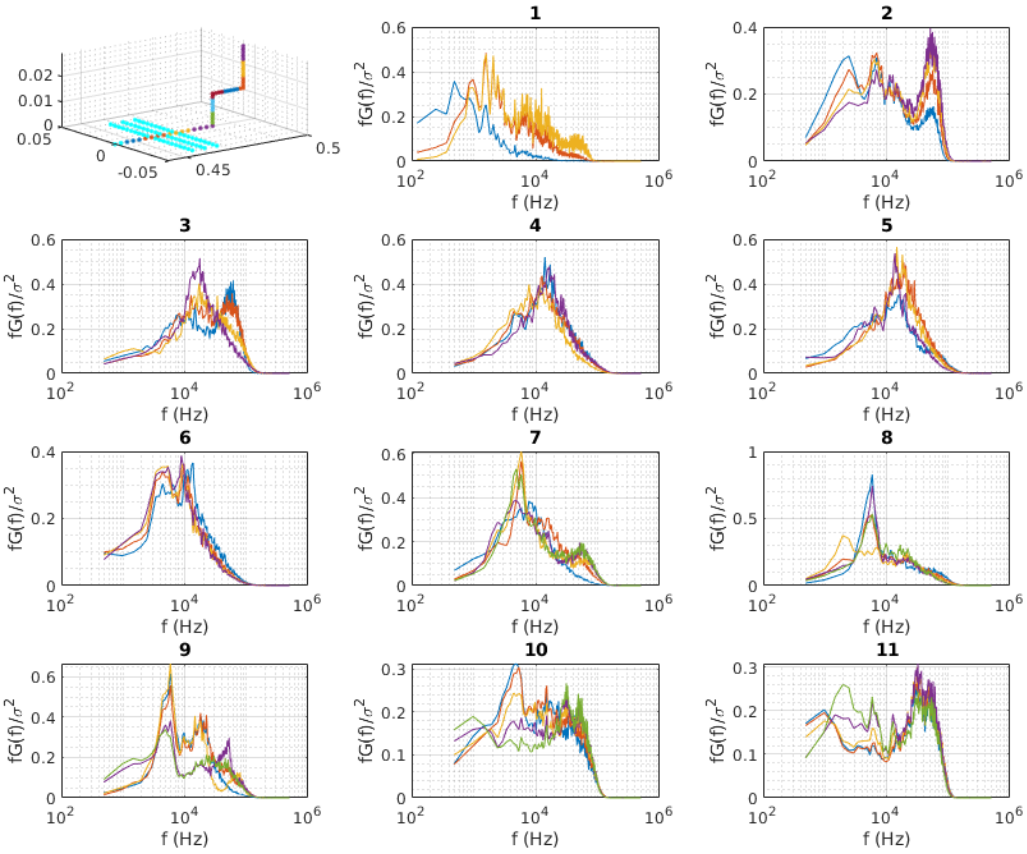

Figure 3.8 Power spectral density for cylinder-fairing flow.

3.2 Spectral Analysis

The power spectral densities are displayed as a semi-logarithmic plot of the frequency and the frequency multiplied by the power density. Showing the power spectral densities in this fashion with the normalized y-axis displays which frequencies have the highest energy content comprising the pressure fluctuations. Using Matlab, the pwelch function was employed to calculate the spectra. The signal was split into at least 8 windows and up to 64 depending on whether or not there was low frequency content that needed to be captured. The advantage to using more windows is that the spectral densities are less noisy and easier to observe and analyze, but the trade-off is the lack of ability to capture lower frequency content as the number of windows increase. Changing the overlap did not significantly change the results, so the default value of 50 percent was kept. The order of the points in each plot follow Matlab's default graph colors going downstream; blue, red, yellow, purple, then green, etc. The first Subplots of each case show the points closest to the undisturbed boundary layer flow. For the first two points in Subplot 1 of the cylinder case and the first point in the cylinder-fairing case, the low-frequency dominant spectra is characteristic of the region under the shock foot at its lowest intermittency values. While the dominant frequency for the baseline cylinder was about 250 Hz, the low frequency content for the cylinder-gap case was about 500 Hz. This can be seen in Subplot 2 of Fig. 3.6, which shows the shock foot being further downstream than the other cases, as expected. The first two points in Subplot 1 of the cylinder-gap case show the spectral densities of the undisturbed turbulent boundary layer, which consists of content at a lower frequency near 5 kHz and a higher frequency over 100 kHz. For taps under the shock foot, a peak can be seen at 4 to 6 kHz, depending on the case. As the intermittency increases, a second peak at a higher frequency forms and grows near 50 kHz. This can be seen in Subplot 2 of both Fig. 3.6 and Fig. 3.8, as well as Subplot 3 of Fig. 3.7. The characteristic shape of the bimodal spectra near the shock foot resembles experimental data collected in the past [1, 13]. For tap locations behind the shock foot, the low frequency peak shrinks slowly, but the high frequency peak grows quickly. This behavior is most evident in the baseline cylinder case but can still be observed in the other cases, particularly the growth of the high frequency peak. Continuing downstream, once the flow

has separated behind the shock, the dual-peak characteristic persists with the high frequency content remaining dominant. As the flow reattaches the spectrum evolves into a single peak at a frequency ranging from about 10 kHz for the baseline cylinder case to about 20 kHz for the cylinder-gap case. The dominant frequency for the cylinder-gap case in this region is noticeably higher compared to the baseline cylinder case, whereas the cylinder-fairing case is in between. This Gaussian shape persists as the flow continues downstream underneath the vortex structures, with some minor variation. For tap locations near the root of the fairing and the characteristics differ more between each case as the group numbers correspond to different parts of the geometry of the fairing and gap. Moving are attention to the face of the cylinder, the spectra show similar characteristics again in the last groups, with a growing peak at between 10 to 20 kHz once again. As a general observation, the dominant frequencies in the power spectra are higher for the cylinder-gap case in the region in front of the cylinder, but are close to the same across the board on the cylinder surface.

3.3 Comparison with Experiment

Experimental data collected by pressure-sensitive paint were collected by Garner and Schmisseur as a series of images of the flatplate in front of the cylinder viewed from the top [6]. The spark Schlieren photographs taken from the experiment are presented in Fig. 3.9. The numerical Schlieren images from the computation that are presented in Fig. 3.10 qualitatively match the experimental data rather well. The mean pressure along the centerlines along the floor of the experiment and computation are presented in Fig. 3.11. Although quantitatively different, the mean pressures along the centerline have the same characteristic shape as those found in literature [3, 5, 8]. The comparison of the RMS of the pressure variations is presented in Fig. 3.12. While the initial peak in these plots correspond to the mean location of the shock foot, the second peak and inflection closer to the root corresponds to the area underneath the vortex near reattachment. The values in the undisturbed boundary layer for the computation appeared to be lower in every case, whereas the initial pressure increase seemed to overshoot. In addition, the shock foot was slightly farther upstream in

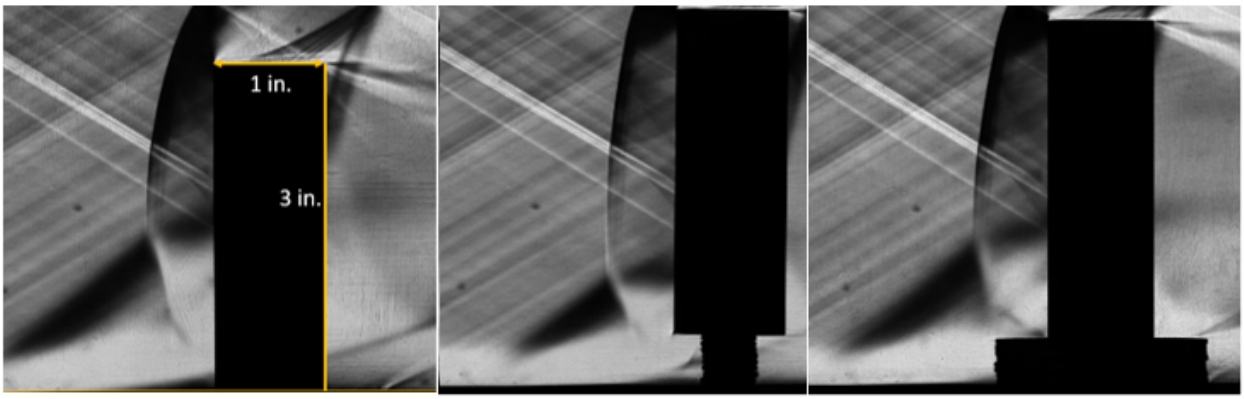

Figure 3.9 Spark Schlieren photographs for each case.

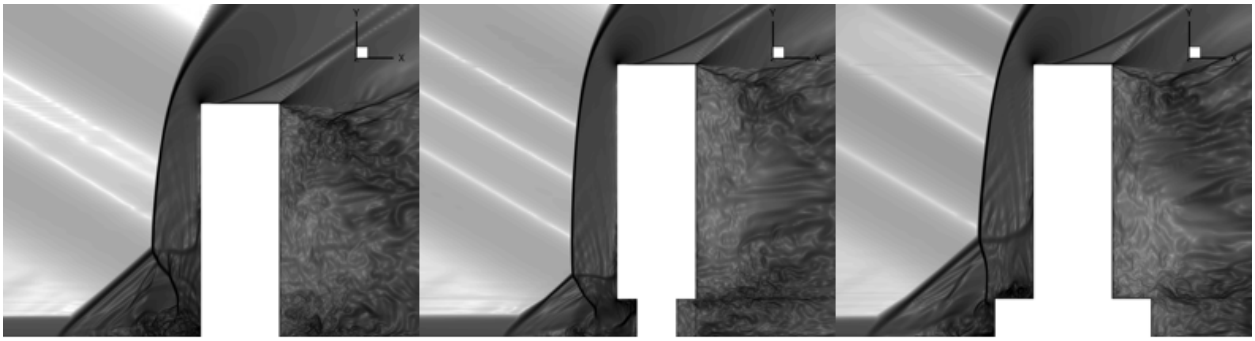

Figure 3.10 Numerical Schlieren profiles from computation for each case.

the experiment. Overall, the differences are consistent with each case, and can all be likely attributed to the same factors, which will be elaborated on later.

The power spectra for pressure were compared as well, as presented in Figs. 3.13-3.15. The first tap of each group as presented in Table 2.2 were compared to the corresponding points in the experimental images. Generally, the experimental data displayed broadband power spectral densities, with no evidence of a double peak anywhere in the flow. Near the areas of intermittency and into the separated region, the peaks of the experimental spectra align with the higher-frequency mode in the computational spectra. However, the expected lower-frequency mode shown in the computation does not appear in the experiment. The baseline cylinder case shows an increasing high-frequency dominance that was not apparent in the other two cases. In some of the locations in the reattachment region under the vortex, there seems to just be an offset in the peak frequency about half of an order of magnitude.

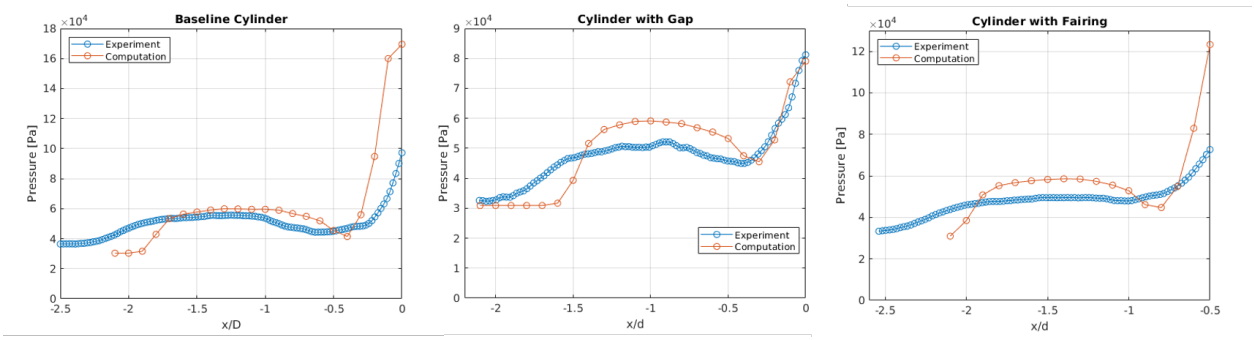

Figure 3.11 Comparison of mean pressure along centerline with experiment.

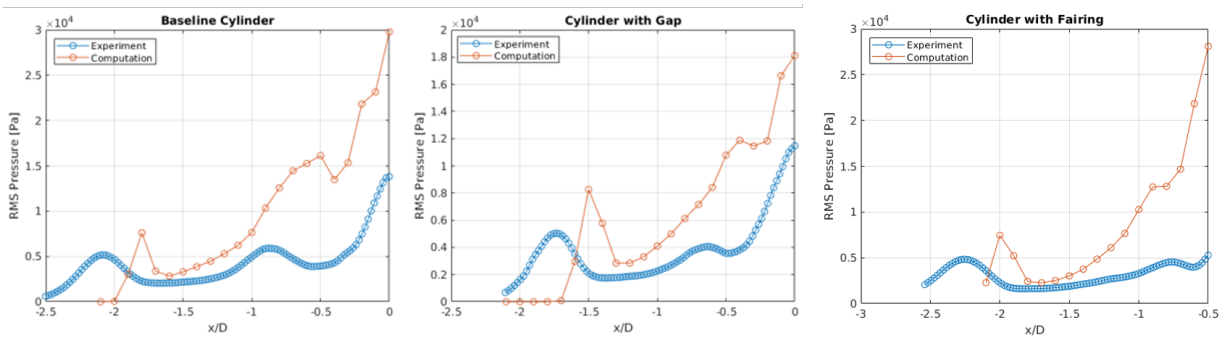

Figure 3.12 Comparison of RMS pressure along cenerline with experiment.

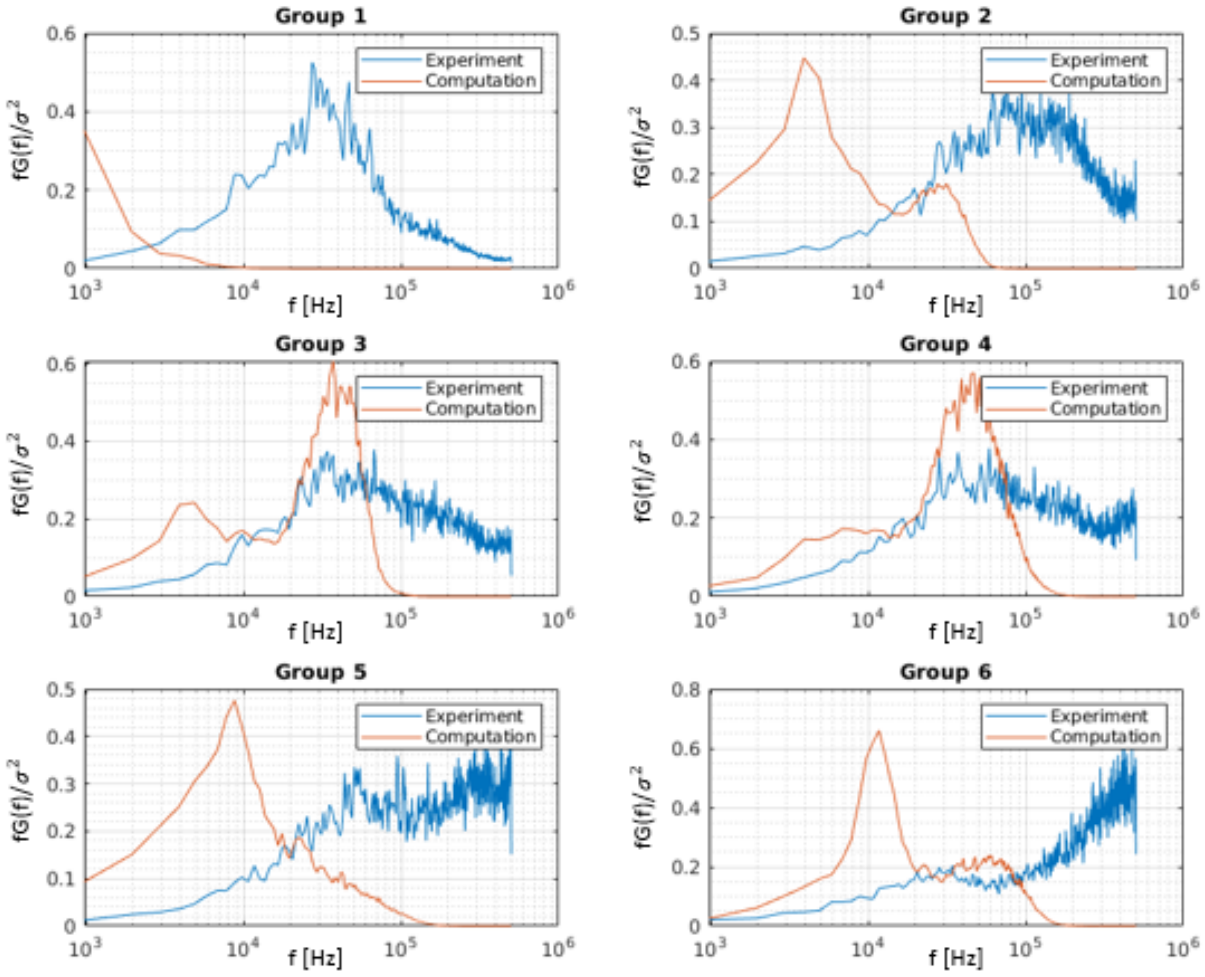

Figure 3.13 Power spectral densities of baseline cylinder case.

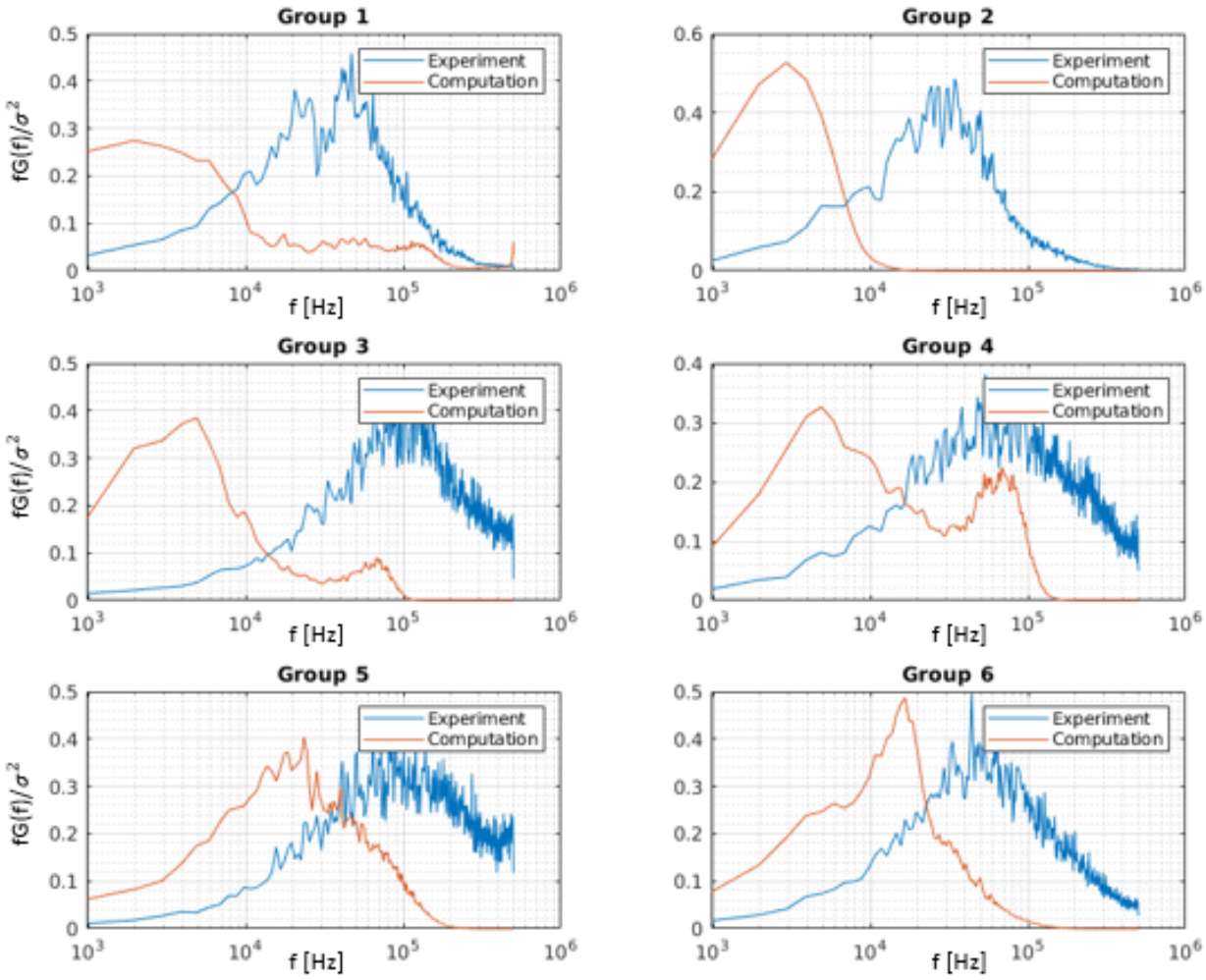

Figure 3.14 Power spectral densities of cylinder-gap case.

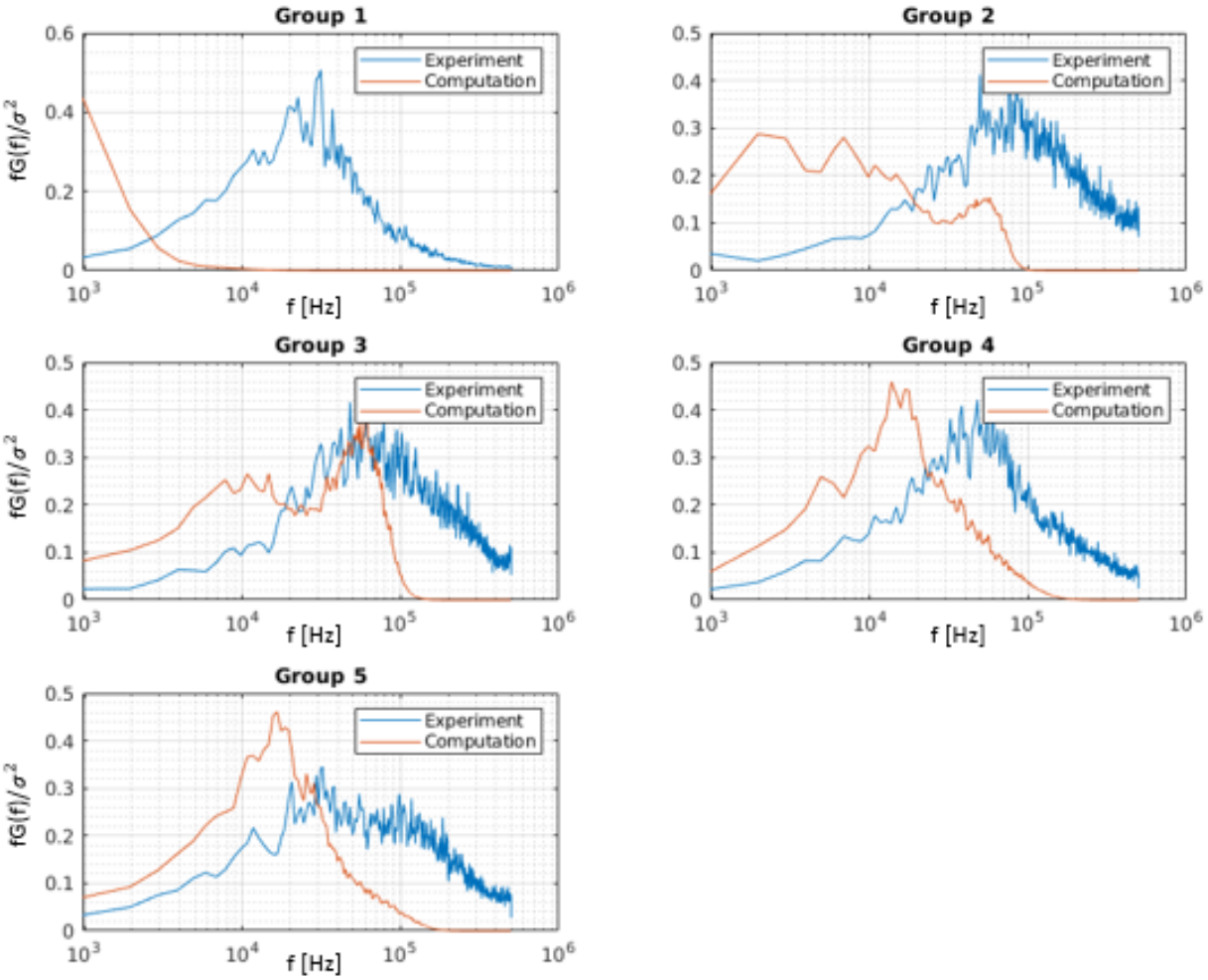

Figure 3.15 Power spectral densities of cylinder-fairing case.

Reasons for discrepancy could be attributed to several factors, including the difference in boundary layer thicknesses, the inherent biases of the pressure-sensitive paint, the lack of resolved turbulence in the computed incoming boundary layer, and the inability of the turbulence model to capture non-equilibrium effects. While the dimensions of the overall flow domain of the experiment and computation resembled each other, the reported boundary layer thickness in the wind tunnel, about 11 mm, was about twice as thick as the computation, at only 5.57 mm taken at the location in front of the shock at $x/d = -2.5$. In addition, the boundary layer was fully turbulent in the wind tunnel from the start, whereas it was initially laminar at the inlet and transitioned after about 1.1 inches (0.028 meters) on the flat plate for the computation. However, the PSP that was used to collect pressure fluctuation data over time was not entirely without limitations. The experimental data to not exhibit the lower frequency content at all in the power spectra, and do not display the bimodal distribution in the intermittent region. Pressure-sensitive paint tends to degrade over time and be affected by other variables such as temperature.

An attempt was made to nondimensionalize the frequency using the Strouhal number using length scales based off the differing boundary layer thickness. Although the peaks in the initial separated shock region seemed to line up, the peaks of the spectra under the turbulent votrices and close to the cylinder-wall juncture do not. Because both the peak frequency in the experiments and the length scales were already greater than the computation near the root, nondimensionalizing only further increased the disparity in the region. A sample calculation of the nondimensionalization for the cylinder-gap case is presented in Table 3.1, where the boundary layer thickness was taken at $x/d = -2.5$. The largest discrepancy between the experimental cases was the behavior near the cylinder wall juncture, where there was massively higher frequency content by an order of magnitude in the baseline cylinder that was not evident in any way for the other experimental runs.

3.4 Two-Point Correlations

The two-point correlations for the taps are presented in an analogous arrangement as the spectral plots, with normalized cross-correlation plotted against the time delay. As previously

Table 3.1 Strouhal number calculation on cylinder-gap case for Group 6.

Variable	Computation	Experiment
Boundary Layer Thickness [m]	5.57e-3	1.10e-2
Freestream velocity [m/s]	510	507
Initial Peak Frequency [kHz]	16.6	43.9
Peak Strouhal Number	0.182	0.957

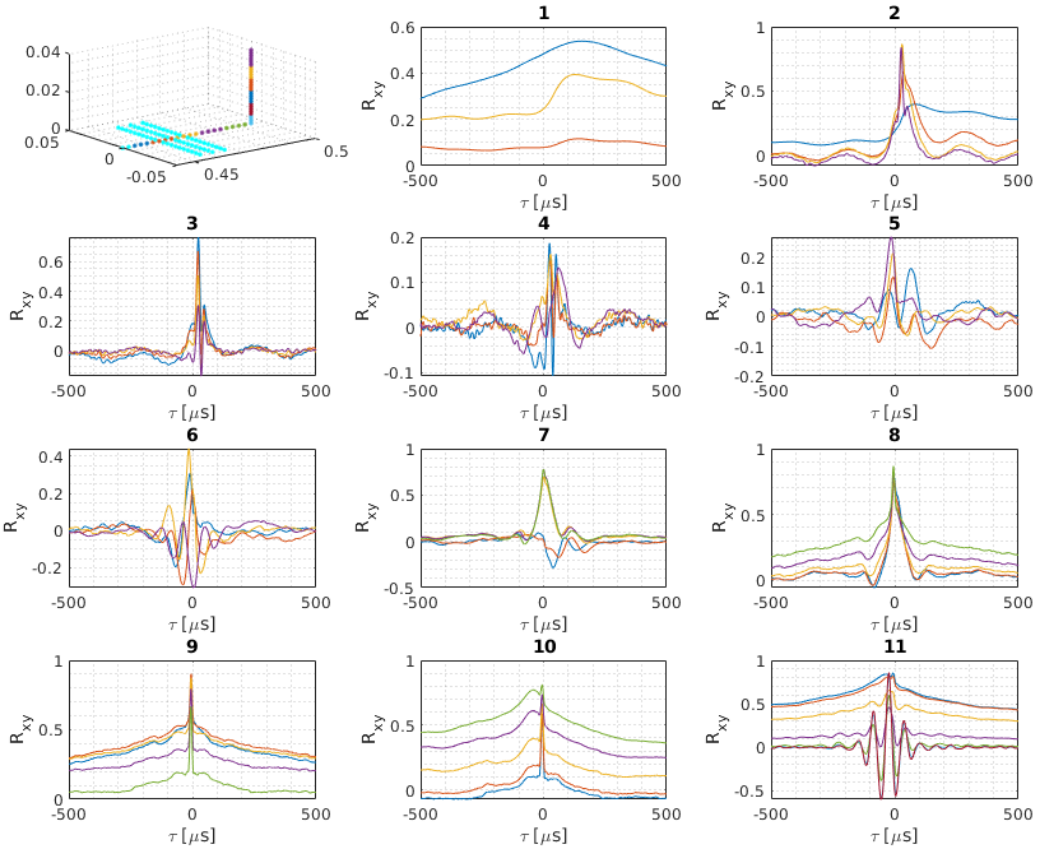

Figure 3.16 Cross-correlations for baseline cylinder flow.

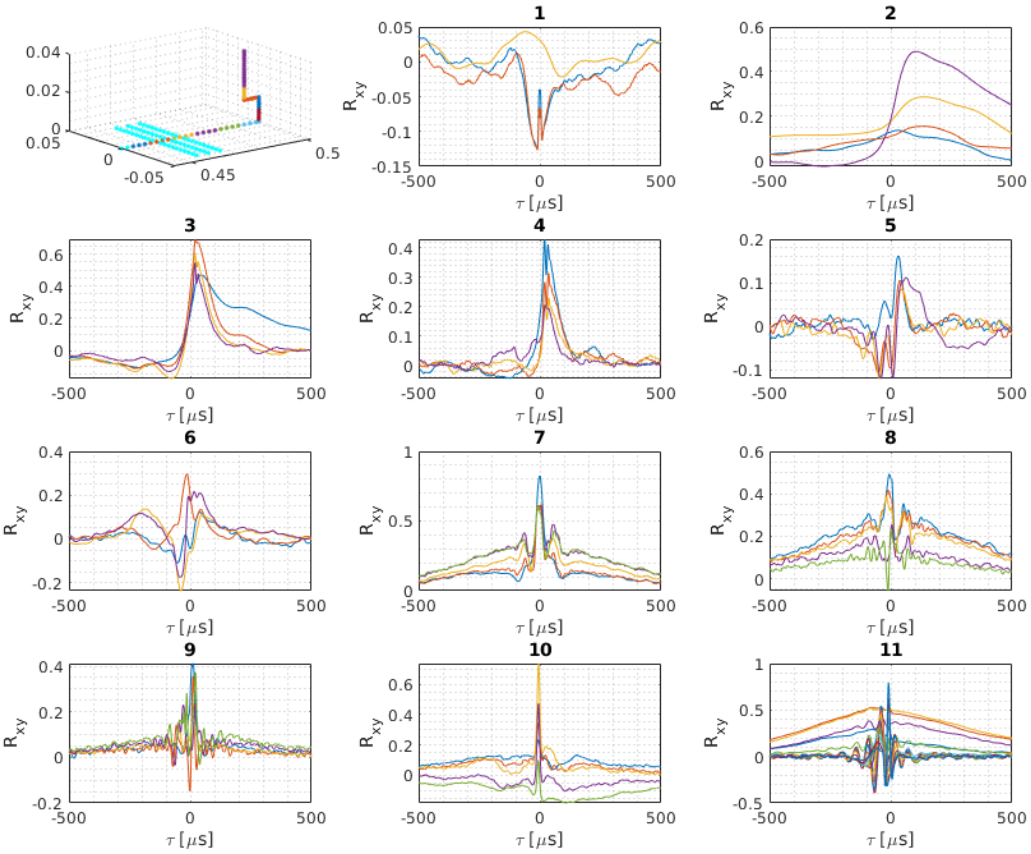

Figure 3.17 Cross-correlations for cylinder-gap flow.

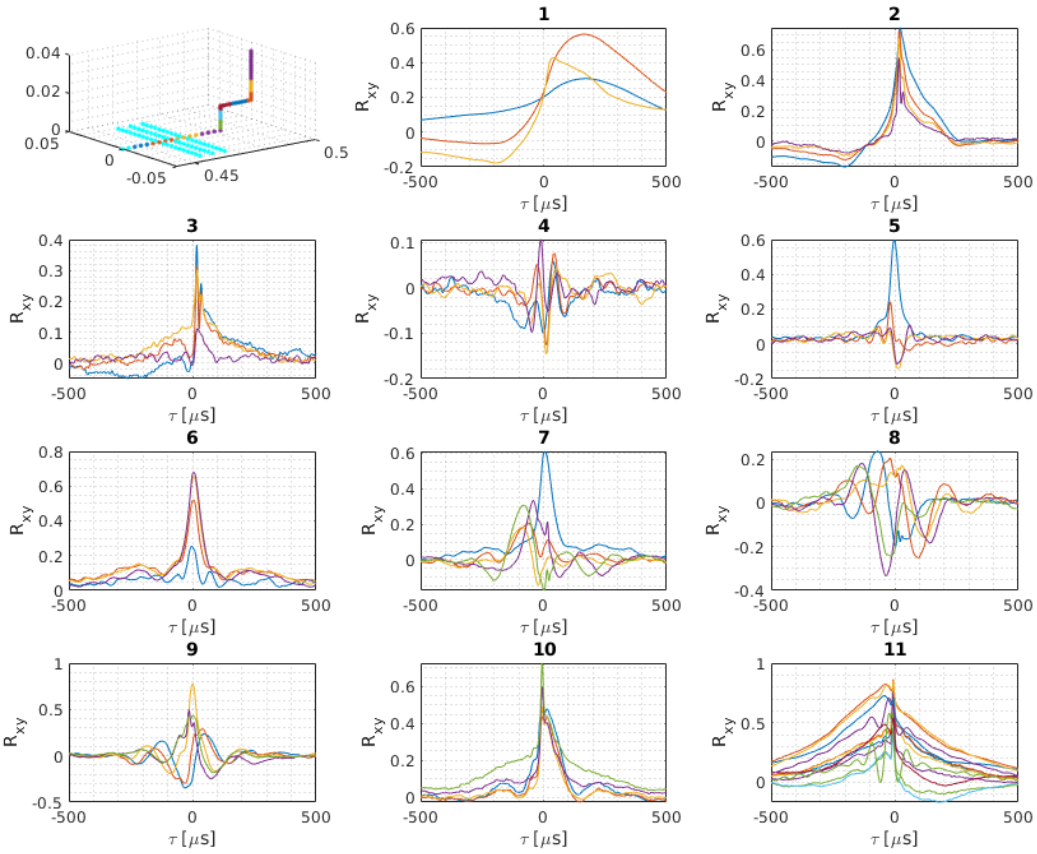

Figure 3.18 Cross-correlations for cylinder-fairing flow.

stated, each point was correlated with the tap two spaces upstream of it. The Matlab function used was xcovs, taking the two raw pressure signals as the input. The correlations about the shock foot are characterized buy a smooth jump in the R_{xy} value and then falling gradually after a slight time delay. In the initial separated region, the correlations seem fairly strong. The strength of the correlations fall in the unsteady, turbulent reattachment area behind the shock. Between each of the cases, the correlations have a similar characteristic with a sharp peak up until they reach a corner, where each case shows more complex variation in those areas. Underneath the horseshoe vortex closer to the root, the optimal time delay becomes negative, indicating reversed flow. Another area of interest is the impingement of the shock on the cylinder surfaces, where the shape consists of one similar to that of directly behind the shock foot, with a somewhat sharp peak. This can be observed more clearly on the baseline cylinder case in Subplot 8 of Fig. 3.16. The surface of the cylinder is also characterized by a fluctuating rise and fall in a broadband correlation, interrupted by a persisting sharp peak that is the convection velocity. These features are bit harder to see in Fig. 3.17 and Fig. 3.18 as most of them are clumped into the last Subplot. Other features of the cross-correlations can be seen in the Subplots, but the geometries differ, and the characteristics are expected to be different as well.

Some spanwise two-point correlations for each case can be seen in Fig. 3.20-3.22. Three horizontal arrangements of taps were extracted in varying locations relative to the shock foot location for the cylinder-gap case. The front row was located in front of the shock, the second row approximately below the area beneath the shock foot, and the back row behind the shock, as shown in Fig. 3.19. Each row was divided into 4 groups of 5 taps each (not including the centerline tap), and the Subplots in each figure show the groups in order going left to right, back to front. Similar to before, each point was correlated with the point 2 spaces to the right of it. The locations where it jumps from the end of the row to the start of the next can be seen in Subplots 4 and 8, where the correlation is expected to be close to 0. The jumps across the centerline can be observed in Subplots 2, 6, and 10, where two of the correlations vary slightly from the other three. As there are only 11 groups shown, the last group of 5 taps in the bottom right are not shown in the Subplots, where the last 2 points would have been correlated to the freestream centerline taps. Aside from the exceptions as

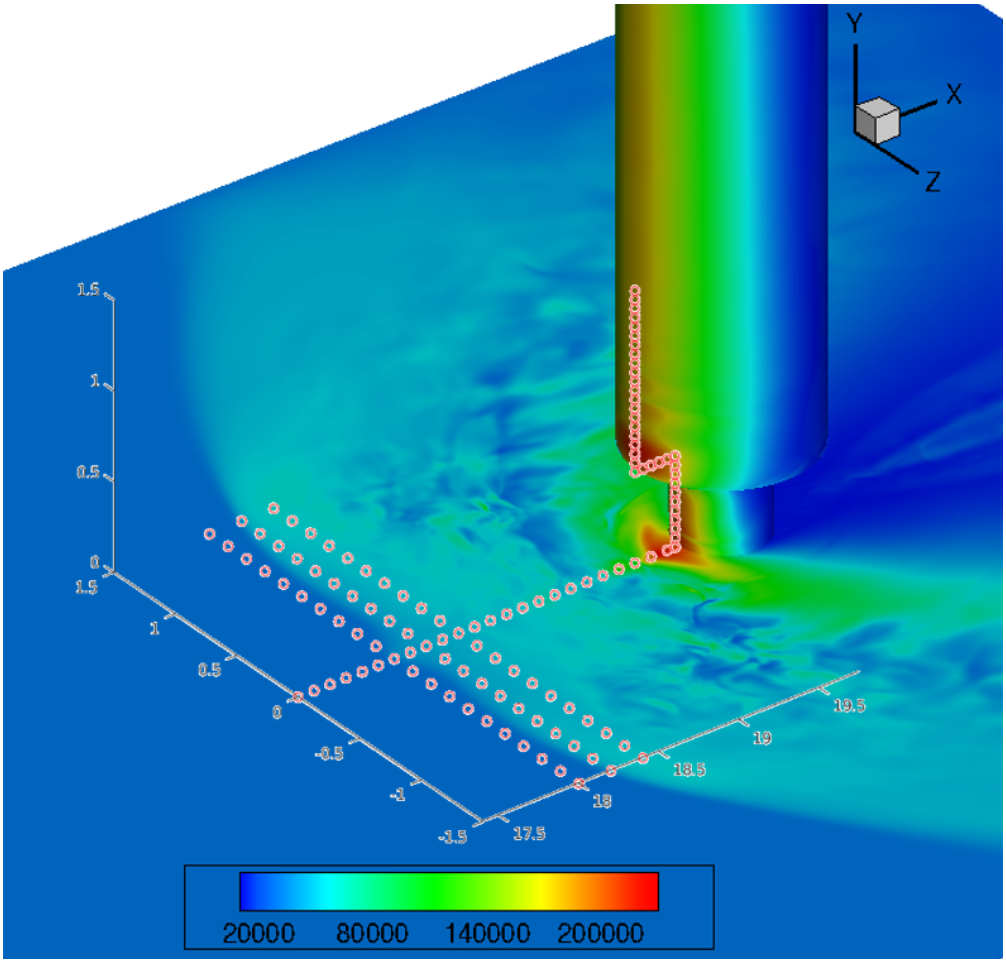

Figure 3.19 Tap locations on pressure contour for cylinder-gap case.

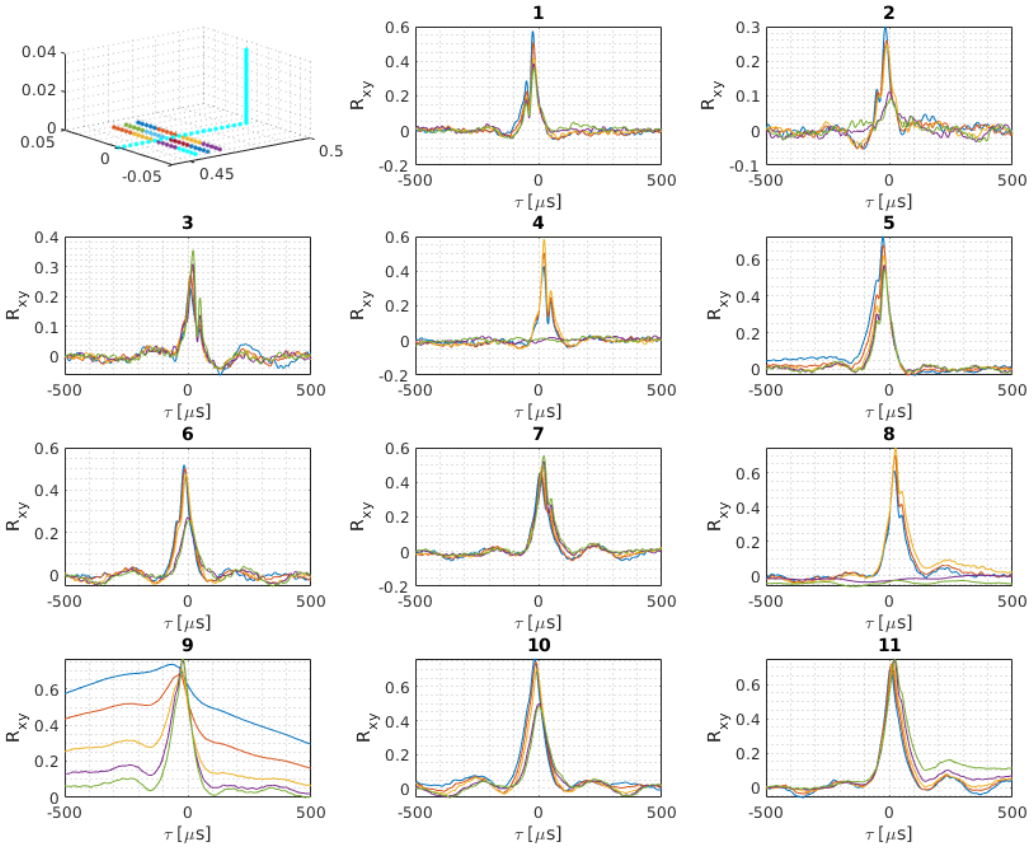

Figure 3.20 Span-wise cross-correlations for baseline cylinder flow.

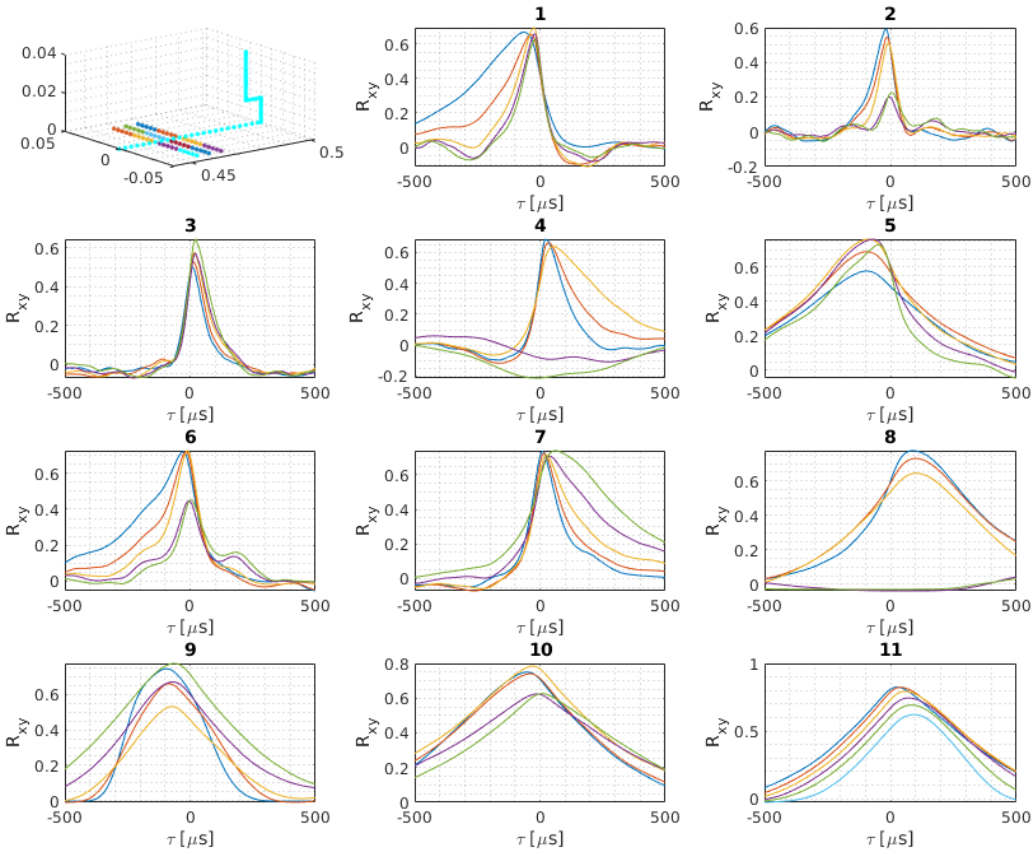

Figure 3.21 Span-wise cross-correlations for cylinder-gap flow.

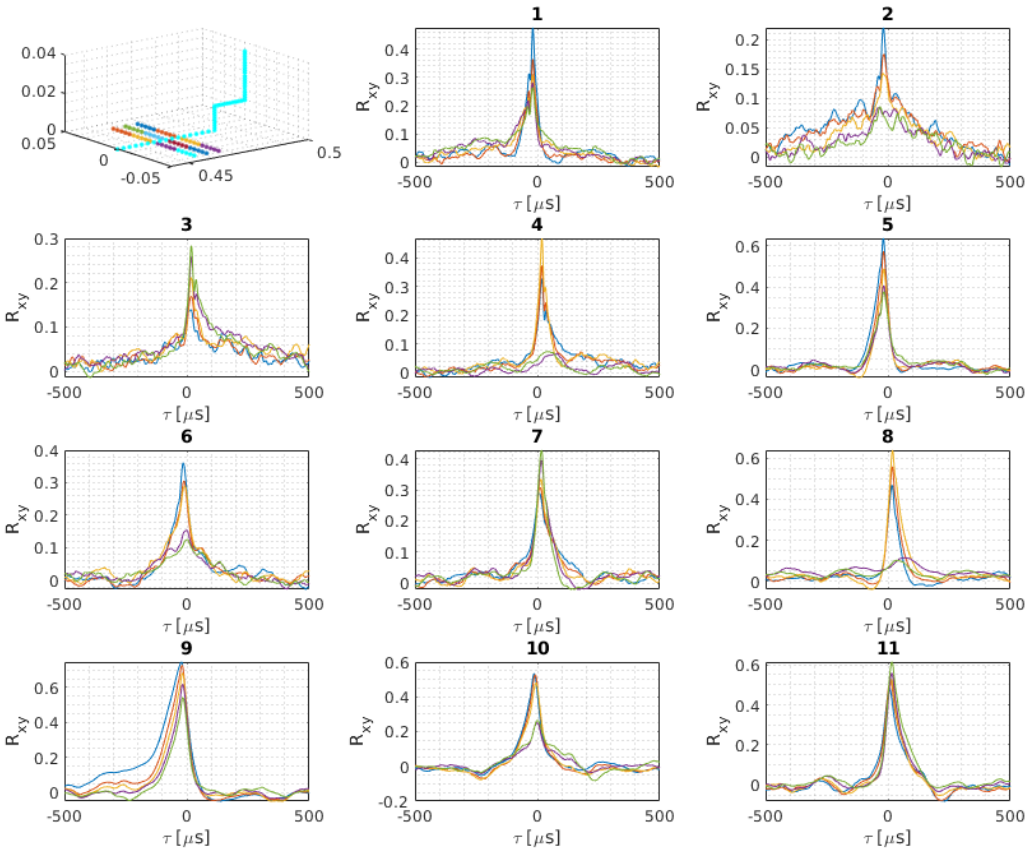

Figure 3.22 Span-wise cross-correlations for cylinder-fairing flow.

explained, the correlations have a similar general smooth shape, being broader behind the shock and sharper in front. The strength of the correlation only varies slightly on either side of the shock for the cylinder-gap case in Fig. 3.21, all with values generally peaking between 0.6 and 0.8. Since all the tap locations between each of the three cases are in the same location, the horizontal arrangements are all behind the shock for the baseline cylinder and cylinder-fairing case. The strength in the correlation drops when the flow separates, as can be observed in Subplot 2 and 3 of Fig. 3.20 and Subplots 1-4, 6, and 7 of Fig. 3.22. By extending the base of the cylinder outward while keeping the taps stationary, the different cases effectively illustrate different regions on the wall relative to the shock and separation locations. The greatest change in the correlation strength can be observed in the fairing case, where the value changes from 0.6 to 0.2 as the taps move from behind the shock into the region of separated flow.

The next figures show the two-point correlations with the point located on the centerline in the middle row. Since the correlations are taken from each point to the middle, negative time-delay peaks will be observed for the first four Subplots, and positive peaks will be observed for the last three Subplots. In general, the correlation is stronger the closer the point is to the center, and stronger before the separation vortex. The propagation of the peaks can be observed in the Subplots, where as the distance increases, the correlation strength decreases as the time-delay increases. With the baseline cylinder case, Fig. 3.23 shows some degree of plausible correlation in all but Subplots 1, 4, and 8. For Subplots 1 and 4, the region of the varying points begin to enter the more separated area of the flow. Subplot 8 does not show a distinct peak even though Subplot 5 shows a weak correlation that can be definitively seen propagating. Most of the correlations for the cylinder-gap case shown in Fig. 3.24 exhibit broadband characteristics. The correlative peak starts out negative in Subplot 1 and can be seen cohesively propagating in subsequent Subplots. Although more defined than the baseline cylinder case, the correlations for the cylinder-gap case still have a lack of symmetry with Subplots 5 and 8. With the cylinder-fairing case, Fig. 3.25 shows the general lack of correlation in the fully separated region with the early plots and stronger correlation early into the separation with the later plots. In all the cases, there appear to be some bias that favors the left side when it comes to correlation strength. This could be

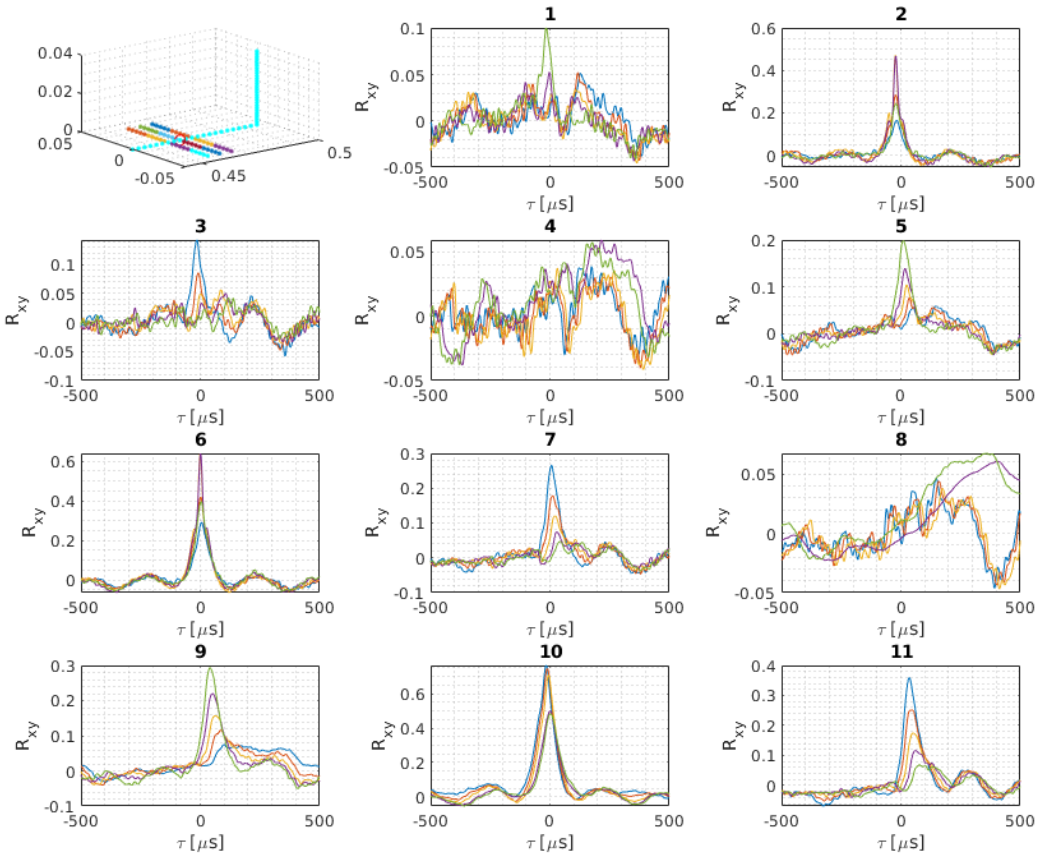

Figure 3.23 Cross-correlations with fixed point for baseline cylinder case.

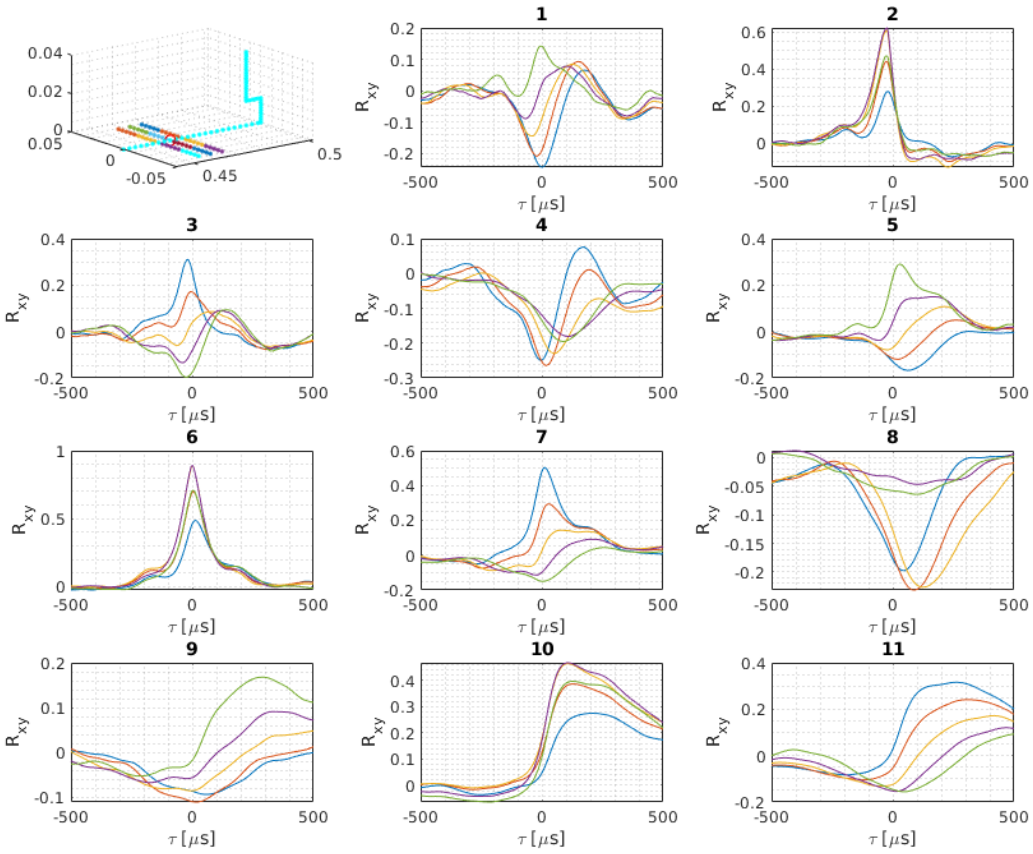

Figure 3.24 Cross-correlations with fixed point for cylinder-gap case.

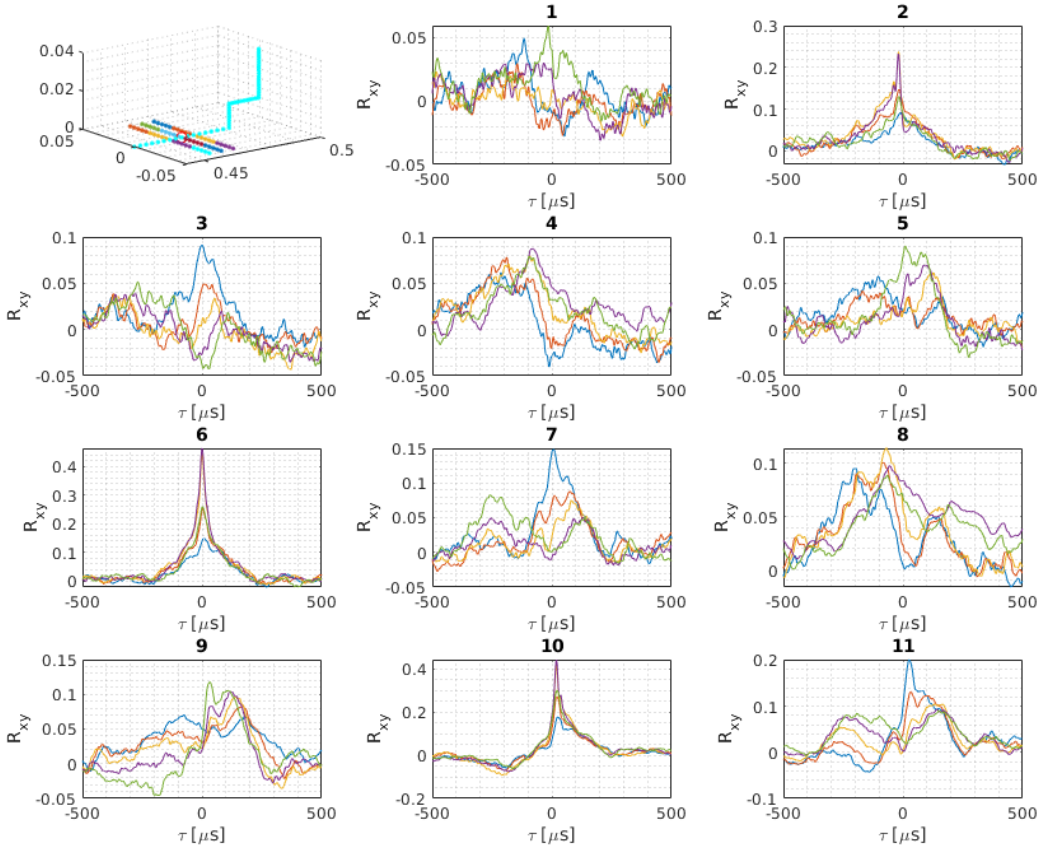

Figure 3.25 Cross-correlations with fixed point for cylinder-fairing case.

due to grid points existing exactly on the centerline, but the computation did not keep a steady stagnation point, and effectively treated the centerline as part of the left half of the flow domain.

4. CONCLUSION

Flow near a cylinder-wall juncture was examined and the effect of geometric details was explored by introducing a gap or fairing at the cylinder root. These geometric alterations modified the flow field considerably. Flow visualization illustrated different wave patterns and areas of heating for each case. Although the gap case shows evidence of higher wall heat flux values on the bottom half of the main cylinder body, the fluctuations in the wake are more predictable. The fairing case does not subject the cylinder to as much heating, but has high values in small patches on the wall and top surface of the fairing in front of the cylinder. Time-series data at specified tap locations were taken for each case and power spectral densities and two-point correlations were compared. The data seemed to have similar characteristics to those reported in the available literature for the the baseline cylinder case. Comparing with experimental data, there seem to be noticeable quantitative differences with the mean and RMS pressure values on the centerline, but the curves are qualitatively similar. However, there seems to be greater discrepancy in the spectral analysis. An immediate change in the computational side that could help the improve the computations would be to impose the thicker boundary layer. In terms of flow control, changing the geometry near the wall juncture produced significant differences in the locations of the shock foot and frequencies of the pressure fluctuations.

The intention is to expand on the simple geometries, such as using a blunt fin in place of the cylinder. From past studies, the diameter of the leading edge of a fin has the most impact on the flow field, so comparing cases with a cylinder is a good starting point. Another step to take would be smoothing the gap and fairing to make the geometry change gradual rather then have 90 degree corners. The results from the smoother geometries would produce drastically different results primarily at the edges with corner flows. Another goal that would require more computation time would be to calculate variables such as wall heat flux or skin friction from the taps by extracting several more points above each tap in the y-direction. Variables like those are not directly outputted via taps by KCFD and must be calculated afterward. Temperature and pressure gradient values can be extracted with the desired order

of accuracy at each tap location rather than needing to compute the whole domain over a long sample time.

Bibliography

[1] L. Brusniak and D.S. Dolling. "Physics of unsteady blunt-fin-induced shock wave/turbulent boundary layer interactions". *Journal of Fluid Mechanics* 273 (1994), pp. 375–409.

[2] D. S. Dolling and C. T. Or. "Unsteadiness of the Shock Wave Structure in Attached and Separated Compression Ramp Flows". *Experiments in Fluids* 3 (1) (1985), pp. 24–32.

[3] D.S. Dolling and S.M. Bogdonoff. "An experimental investigation of the unsteady behavior of blunt fin-induced shock wave turbulent boundary layer interactions". *Princeton Univsersity Report* (1982).

[4] D.S. Dolling and S.M. Bogdonoff. "Blunt Fin-Induced Shock Wave/Turbulent Boundary-Layer Interaction". *AIAA Journal* 20 (12) (1982), pp. 1674–1680.

[5] D.S. Dolling and S.M. Bogdonoff. "Scaling of Interactions of Cylinders with Supersonic Turbulent Boundary Layers". *AIAA Journal* 19 (1991), pp. 655–657.

[6] A.N. Garner. "Characterizing the Effect of Base Gaps on Shock Wave/Boundary-Layer Interactions using Unsteady Pressure-Sensitive Paint". MA thesis. University of Tennessee Space Institute, 2020.

[7] AL Kistler. "Fluctuating Wall Pressure Under a Separated Supersonic Flow". *Acoustical Society of America* 36 (3) (1964), pp. 543–550.

[8] B. Lakshmanan and S. N. Tiwari. "Investigation of Three-Dimensional Separation at Wing/Body Junctions in Supersonic Flows". *Journal of Aircraft* 31 (1) (1994), pp. 65–71.

[9] B. Lakshmanan and S. N. Tiwari. "Study of Supersonic Intersection Flowfield at Modified Wing-Body Junctions". *AIAA Journal* 31 (5) (1993), pp. 877–883.

[10] J. Larson and S. Kawai. "Wall-Modeling in Large Eddy Simulation: Length Scales, Grid Resolution and Accuracy". *Center for Turbulence Research* (2010), pp. 39–46.

[11] J. Poggie, N.J. Bisek, and R.L. Kimmel. “Spectral Characteristics of Separation Shock Unsteadiness”. *AIAA Journal* 53 (1) (2015), pp. 200–214.

[12] G.S. Settles. “An Experimental Study of Compressible Turbulent Boundary Layer Separation at High Reynolds Number”. PhD thesis. Princeton University, 1976.

[13] F.O. Thomas, C.M. Putnam, and H.C. Chu. “On the Mechanism of Unsteady Shock Oscillation in Shock Wave/Turbulent Boundary Layer Interactions”. *Experiments in Fluids* 18 (1) (1994), pp. 69–81.

[14] H. Zhang and R.K. Agarwal. “Application of Quadratic Constitutive Relation to One-Equation k-kL Turbulence Model kL Turbulence Model”. *Mechanical Engineering and Materials Science Independent Study* 106 (2019), pp. 1–14.